Drosophila ClC-a is required in glia of the stem cell niche for proper neurogenic proliferation and wiring of neural circuits.

Haritz Plazaola-Sasieta[1], Qi Zhu[1], Héctor Gaitán-Peñas[2,3], Martín Rios[1], Raúl Estévez[2,3], Marta Morey[1,4 *]

[1]Departament de Genètica, Microbiologia i Estadística, Facultat de Biologia, Universitat de Barcelona, Barcelona, Spain

[2]Departament de Ciencies Fisiològiques, Genes, Disease and Therapy Program IDIBELL-Institute of Neurosciences, Universitat de Barcelona, L'Hospitalet de Llobregat, Spain

[3]Centro de Investigación Biomédica en Red de Enfermedades Raras (CIBERER), Instituto de Salud Carlos III, Madrid, Spain

[4]Institut de Biomedicina de la Universitat de Barcelona (IBUB), Barcelona, Spain

* Corresponding Author

ABSTRACT

Glial cells form part of the neural stem cell niche and express a wide variety of ion channels; however, the contribution of these channels to nervous system development is poorly understood. We explored the function of the *Drosophila ClC-a* chloride channel, since its mammalian ortholog *CLCN2* is expressed in glial cells, and defective channel function results in leukodystrophies, which in humans are accompanied by cognitive impairment. We found that *ClC-a* was expressed in the niche in cortex glia, which are closely associated with neurogenic tissues. Characterization of loss-of-function *ClC-a* mutants revealed that these animals had smaller brains and widespread wiring defects. We showed that *ClC-a* is required in cortex glia for neuroepithelia and neuroblast proliferation and identified defects in a neuroblast lineage that generates guidepost glial cells essential for photoreceptor axon guidance. We propose that glia-mediated ionic homeostasis could non-autonomously affect neurogenesis, and consequently, the correct assembly of neural circuits.

INTRODUCTION

The remarkable proliferative capacity of stem cells requires tight regulation to ensure generation of the appropriate amount of cells and tissue homeostasis during development. This regulation is controlled not only by stem cell-intrinsic programs, but also by extrinsic cues from the surrounding cellular niche. In vertebrate and invertebrate nervous systems, glia form part of the niche for neural stem/progenitor cells (Bjornsson et al., 2015; Ruddy and Morshead, 2018). In both systems, the effect of glia on neurogenic tissues has mainly been related to the secretion of factors that regulate the maintenance, proliferation, and differentiation of stem and progenitor cells.

One of the findings that changed the earlier view of glia as simply a passive structural element was the observation that glial cells expressed a wide variety of ion channels and neurotransmitter receptors (Barres, 1991; Barres et al., 1990). Although the physiological roles of several of these ion channels in glia have been described both in normal and pathological states of the mature nervous system (Black and Waxman, 2013; Nwaobi et al., 2016; Olsen et al., 2015; Pappalardo et al., 2016; Verkhrastsky and Steinhauser, 2000), the contribution of glial ion channel functions specifically in the niche during nervous system development remains poorly understood.

Among the ion channels expressed in glia, the vertebrate ClC-2 chloride channel has been proposed as one of the channels involved in K^+ buffering, a key ionic homeostasis process in which glia are involved (Wang et al., 2017, Jentsch and Pusch, 2018). In the mature nervous system, increased neural activity leads to an increase in extracellular K^+, which can alter neuronal excitability. To lower the concentration of K^+, astrocytes take up the ion and distribute it to distant sites via the astrocytic syncytia. Uptake of K^+

57 occurs concomitantly with uptake of Cl^- and water, producing transient astrocyte
58 swelling (Bellot-Saez et al., 2017). Based on its expression in astrocytic glia, the ClC-2
59 channel has been proposed as one of the channels that might participate in this Cl^-
60 uptake (Blanz et al., 2007; Hoegg-Beiler et al., 2014; Sirisi et al., 2017). Mutations in
61 *CLCN2, which codes for* ClC-2*,* are responsible for leukoencephalopathy with ataxia
62 (LKPAT) (Depienne et al., 2013) and ClC-2 has been related to megalencephalic
63 leukoencephalopathy with subcortical cysts (MLC) (Hoegg-Beiler et al., 2014;
64 Jeworutzki et al., 2012; Sirisi et al., 2017). Both conditions are characterized by
65 vacuolization of white matter and edema, most probably as a consequence of impaired
66 K^+ buffering, but patients can also present learning disabilities and mild to moderate
67 intellectual impairment. The finding that ClC-2 is expressed during development in glial
68 precursors and is required for their differentiation (Hou et al., 2018), together with the
69 fact that intellectual impairment can arise from connectivity defects, suggests that this
70 channel may have additional functions during neural development. To explore this
71 possibility, we leveraged the functional parallelisms between vertebrate and *Drosophila*
72 glia (Chotard and Salecker, 2004; Corty and Freeman, 2013; Freeman and Doherty,
73 2006) and used the fly, where neurogenesis has been extensively studied, the niche is
74 simpler than in vertebrates, and the *ClC-a* gene codes for the fly homolog of the
75 vertebrate ClC-2 chloride channel.
76
77 The fly central nervous system contains three structures: the central brain (CB), the
78 ventral nerve cord (VNC), and the optic lobe (OL). The CB and VNC are generated by
79 neural stem cells called neuroblasts that delaminate from the neuroectoderm during
80 embryonic development and give rise to larval and adult brain through two rounds of
81 neurogenesis (Doe, 2008). The OL originates from a group of neuroepithelial cells that

82 proliferates and separates into two crescent shaped primordia, the outer and inner
83 proliferation centers (OPC and IPC), which produce neuroblasts and precursor cells of
84 the different visual processing centers (Apitz and Salecker, 2014). In addition, the OL
85 has been extensively used as a model to explore neural circuit assembly (Plazaola-
86 Sasieta et al., 2017), primarily because the modular nature and stereotyped development
87 of the fly eye enable easy detection of wiring defects in photoreceptors and other visual
88 system neurons.
89
90 The cellular components in the fly niche comprise the neurogenic cells themselves
91 (neuroepithelia and/or neuroblasts and precursor cells), the newly generated neurons,
92 and three types of glia. Of these latter, the perineural and subperineural glia are
93 components of the blood brain barrier (BBB) that respond to systemic nutritional cues
94 and signal to neuroblasts to proliferate (Chell and Brand, 2010; Kanai et al., 2018;
95 Perez-Gomez et al., 2013; Sousa-Nunes et al., 2011; Spéder and Brand, 2014). Cortex
96 glia are large cells that lie beneath the subperineural glia. Nutritional cues and
97 neuroblast signals alike induce cortex glia remodeling to encase neuroblasts and their
98 immediate progeny in a chamber and older neurons individually (Read, 2018; Spéder
99 and Brand, 2018). This close association protects neuroblasts from oxidative stress and
100 nutritional restriction (Bailey et al., 2015; Cheng et al., 2011), and is essential for
101 neuronal survival (Coutinho-Budd et al., 2017; Dumstrei et al., 2003; Pereanu et al.,
102 2005; Read, 2018; Spéder and Brand, 2018). In the OL, a distinct subtype of cortex glia
103 that expresses miRNA mir-8 (surface associated cortex glia) is in direct contact with the
104 OPC (Morante et al., 2013). These glial cells send signals that regulate expansion of the
105 neuroepithelium and timely transition from neuroepithelium to neuroblast (Morante et
106 al., 2013). Connectivity is also influenced by glial cells in the visual system, where

107 different types control photoreceptor axon pathfinding and targeting (Chotard and
108 Salecker, 2008; Poeck et al., 2001).
109
110 The electrophysiological properties of *Drosophila* ClC-a are very similar to those of its
111 mammalian counterpart (Flores et al., 2009; Jeworutzki et al., 2012). In addition, both
112 ClC-2 and ClC-a are most abundant in epithelia and the brain. ClC-2 has been shown to
113 play a role in transepithelial transport in enterocytes (Catalán et al., 2004). Similarly,
114 *ClC-a* is also expressed in the epithelia of the fly digestive system, and is involved in
115 transepithelial transport in stellate cells of the Malpighian tubules, the fly secretory
116 system (Cabrero et al., 2014; Denholm et al., 2013). In the vertebrate brain, besides glia,
117 ClC-2 is also expressed in inhibitory neurons, where it regulates neuronal excitability
118 (Földy et al., 2010; Ratte and Prescott, 2011; Rinke et al., 2010). We were interested in
119 the observation that *ClC-a* mRNA is expressed in glia in the embryonic fly nervous
120 system (Kearney et al., 2004; Tomancak et al., 2007, 2002) and is highly expressed
121 throughout development of the nervous system (Celniker et al., 2009; Rose et al., 2007),
122 which indicates a possible role of the channel in nervous system development.
123
124 In this study, we analyzed the expression pattern of *Drosophila ClC-a* in the brain,
125 characterized the first loss-of-function mutant alleles of this chloride channel and
126 investigated their effects on development of the nervous system. We found that *ClC-a* is
127 expressed in several types of glia and uncovered a role for this channel in the niche. Its
128 expression in cortex glia, which are in close contact with OPC and IPC neuroepithelial
129 cells and NBs, was necessary for the proper mitotic activity of these neurogenic tissues,
130 as well as for neuron survival. One of the secondary consequences of reduced
131 neuroblast proliferation was the significantly limited production of guidepost glial cells,

132 which gave rise to non-autonomous neural circuit assembly phenotypes in
133 photoreceptors. Both neurogenic and connectivity defects could be rescued by glial-
134 specific expression of the rat ClC-2 vertebrate channel. We propose that the expression
135 of ion channels in the glial niche can shape the development of the nervous system,
136 controlling the number of glia and neurons generated, as well as the connectivity of the
137 latter.
138
139 **RESULTS**
140 ***ClC-a* is expressed in two types of glia in the developing brain: cortex glia and**
141 **ensheathing glia.**
142 To characterize *ClC-a* expression in the developing brain at different larval stages (L1,
143 L2, and L3), we used reporter lines and antibodies. One of these reporter lines expresses
144 GAL4 under the *ClC-a* endogenous regulatory sequences (see below) and recapitulates
145 the previously reported *ClC-a* expression pattern in Malpighian tubule stellate cells
146 observed with an antibody against ClC-a (this study and Cabrero et al., 2014) and a
147 ClC-a protein trap (ClC-a-GFP) (Supplementary Information and Supplementary Figure
148 1A-C). To visualize and monitor *ClC-a* expressing cells throughout development, we
149 combined the *ClC-a-GAL4* line with UAS transgenes that outlined the membrane and
150 labeled the nucleus. *ClC-a* expression was detected in L1 brains on membranes in
151 contact with the developing OPC neuroepithelium (Figure 1A, B). Colocalization of the
152 nuclear RFP signal with the pan glial nuclear marker Repo indicated that *ClC-a* was
153 expressed in a subset of glial cells (Figure 1A, A'). In L2 brains, glial membranes
154 started encasing CB neuroblasts (Figure 1C), and more membrane processes were
155 observed deeper in the brain (Figure 1D). By late L3, the number of ClC-a^{+} glial nuclei
156 in the CB had greatly increased and their glial membranes confined neuroblasts and

157 their lineages in chambers (Figure 1E). A slightly deeper section showed ClC-a$^+$ glial
158 processes forming a smaller mesh (Figure 1F) which ensheathed mature neurons. In the
159 OL, neuroblasts and progenitors were still being produced by the OPC and IPC, which
160 continued to be surrounded by ClC-a$^+$ glial membranes (Figure 1G). We also observed a
161 glial process between the developing lamina (i.e., lamina precursor cells or LPC) and
162 the lobula plug (LoP) (Figure 1H), establishing a boundary between these two regions,
163 which are innervated by neurons of different origin (i.e., photoreceptors generated in the
164 eye disc and innervating the OL through the LPC area, and distal neurons generated
165 from the d-IPC, a region of the IPC) (Figure 1I). Similar expression patterns were
166 observed with anti-ClC-a antibodies and the ClC-a protein trap, confirming the
167 specificity of the *ClC-a-GAL4* driver line in the brain (Supplementary Figure 1D-I).
168
169 We next aimed to identify which types of glial cells expressed *ClC-a*, using cell-type-
170 specific markers and nuclei position. We found that superficial *ClC-a*$^+$ nuclei on top of
171 the OPC neuroepithelium corresponded to a subtype of cortex glia called surface
172 associated cortex glia (Morante et al., 2013), which lie beneath perineural and
173 subperineural glia (Figure 1J). miRNA *mir-8* (Karres et al., 2007), a marker for this
174 subtype of cortex glia (Morante et al., 2013), colocalized with ClC-a protein in cells
175 covering the OPC and the process separating the LPC from the LoP (Figure 1K).
176 Additional experiments indicated that ClC-a$^+$ nuclei present on the surface of the CB
177 and in cortical areas belonged to cortex glia. The membrane and nuclear patterns of
178 ClC-a$^+$ cells were consistent with the nuclear patterns and the membrane scaffold, also
179 known as the trophospongium (Hoyle et al., 1986), observed with the recently described
180 cortex glia driver *wrapper* (Coutinho-Budd et al., 2017) (compare Figure 1G with
181 Figure 1L). In fact, there was extensive colocalization between ClC-a$^+$ and wrapper$^+$

182 membranes in the CB and OL (Figure 1M-N), including surface associated cortex glia
183 on the OPC (Figure 1N, N"). Thus, for the sake of simplicity, we will refer to surface
184 associated cortex glia as cortex glia.
185
186 In order to assess the presence of glial types other than cortex glia, we used an
187 intersectional strategy whereby only ClC-a^{+}/wrapper^{-} cells (i.e., non-cortex glia cells)
188 were labeled. This revealed that *ClC-a* was also expressed in different subtypes of
189 ensheathing glia such as neuropil- and tract-ensheathing glia. *ClC-a* was expressed in
190 neuropil-ensheathing glia surrounding CB neuropils, including the mushroom body
191 calyx (Figure 1O, P). For tract-ensheathing glia, *ClC-a* was expressed in glia around the
192 mushroom body peduncle (Figure 1O), and in the OL in the outer (Xg_o) (Figure 1Q) and
193 inner (Xg_i) (Supplementary Figure 2E-G) chiasm glia, cell types that wrap axonal tracts
194 between the lamina and medulla, and the medulla and lobula complex, respectively. A
195 detailed developmental analysis revealed expression in other glial cells in the OL, as
196 well as in the VNC and peripheral nervous system (Supplementary Figure 2). Most of
197 the ClC-a^{+} glial types observed in the late L3 stage persisted in the adult
198 (Supplementary Figure 2G).
199
200 Together, these data indicate that *ClC-a* is already expressed in early development in
201 cortex glia cells, which are in direct contact with and wrap proliferative tissues such as
202 the neuroepithelia of the OL (OPC, IPC) and neuroblasts in the CB, forming part of the
203 niche. *ClC-a* is also expressed in different types of ensheathing glia whose processes
204 contribute to compartmentalization of the brain by demarcating different neuropils and
205 neuronal tracts.
206

207 **MiMIC insertions in the *ClC-a* locus generate strong loss-of-function alleles.**

208 To explore the role of *ClC-a* in glia, we characterized a set of *Minos*-mediated
209 integration cassette (Mi(MIC)) insertions in the *ClC-a* locus (Figure 2A). This
210 transposon contains a gene trap cassette that leads to the formation of truncated
211 transcripts (Venken et al., 2011) (Figure 2B). We focused on *Mi(MIC)ClC-a*^{05423} and
212 *Mi(MIC)ClC-a*^{14007} alleles (from now on referred to as *05423* and *14007*), since their
213 insertion sites were predicted to interrupt all isoforms of the *ClC-a* gene. The *ClC-a-*
214 *GAL4* line we used was derived from *Mi(MIC)ClC-a*^{05423} by the Gene Disruption
215 Project (Nagarkar-Jaiswal et al., 2015a, 2015b) through recombinase-mediated cassette
216 exchange (RMCE) replacement of the MiMIC gene trap cassette for a GAL4 cassette
217 (Diao et al., 2015) (Figure 2B). Hence, a mutant allele is generated that expresses GAL4
218 under the control of *ClC-a* regulatory sequences. From now on, we will refer to it as
219 *05423*$^{ClC\text{-}a\text{-}GAL4}$. Initial viability characterization of these insertions over deficiency
220 *Df(3R)PS2* (*Df*) revealed the presence of escapers (Supplementary Information).
221 Genetic and mutant phenotype analyses (Supplementary Information and Figure 2G)
222 indicated that allelic combinations could be ordered by strength in the following
223 sequence: *05423*$^{ClC\text{-}a\text{-}GAL4}$*/Df* > *05423/Df* > *14007/Df* = *05423*$^{ClC\text{-}a\text{-}GAL4}$*/14007* >
224 *05423/14007* > *14007/14007*. Since it is difficult to obtain *05423*$^{ClC\text{-}a\text{-}GAL4}$*/Df* or
225 *05423/Df* animals in sufficient numbers, we mainly used *14007/Df* and *05423*$^{ClC\text{-}a\text{-}}$
226 ^{GAL4}*/14007* flies in our experiments. These two allelic combinations behave in a very
227 similar fashion and represent a good compromise in terms of phenotypic strength and
228 mutant animal availability. In addition, the *05423*$^{ClC\text{-}a\text{-}GAL4}$*/14007* combination enables
229 visualization in the mutant background of the glial cells that express *ClC-a* in wild type.
230

231 The predicted loss-of-function nature of the MiMIC insertions characterized was
232 confirmed by immunostaining and western blot. The *ClC-a* expression pattern observed
233 with anti-ClC-a antibody in wild type L3 stellate cells of the Malpighian tubules and
234 brain was not detected in any of the mutant allelic combinations tested (Supplementary
235 Figure 3A-D). Western blots revealed that with a very low frequency, the splice
236 machinery used the endogenous splice acceptor instead of the MiMIC one, and that
237 there was a remnant, albeit very low, of wild type protein in mutants that was only
238 detectable in immunoblots (Supplementary Figure 3E, F).
239
240 In summary, here we have characterized the first *ClC-a* mutants, which are strong loss-
241 of-function alleles.
242
243 **Mutations in *ClC-a* result in smaller brains with photoreceptor guidance defects.**
244 To explore the effect of *ClC-a* mutations on brain development, we started by dissecting
245 adult brains and searching for defects that could have a developmental origin based on
246 *ClC-a* expression patterns in the larval brain. The observation that *ClC-a* was expressed
247 in glia on proliferative tissues in the brain (i.e. neuroepithelia and neuroblasts) led us to
248 hypothesize that mutant brains might be smaller than control ones, and to test this idea
249 we measured OLs from control and mutant animals. We did indeed observe a reduction
250 in OL size in mutants, which was particularly evident in $05423^{ClC\text{-}a\text{-}GAL4}/Df$, the
251 strongest allelic combination, and was also present in $05423^{ClC\text{-}a\text{-}GAL4}/14007$ (Figure 2C)
252 and *14007/Df* (Figure 4H, I).
253
254 Given that we detected *ClC-a* expression in glial processes separating the developing
255 lamina from the LoP and outer chiasm glial cells, we labeled photoreceptors to assess

256 their innervation path. The compound eye of the fly is formed by some 800 units called
257 ommatidia. Each ommatidium contains eight photoreceptors; R1-6, which terminate in
258 the lamina forming the lamina plexus; and R7 and R8, which extend to the medulla. As
259 rows of ommatidia form in the eye disc, photoreceptors extend axons and sequentially
260 innervate the OL. This forms a retinotopic map and each ommatidium in the eye
261 generates a corresponding processing unit in the lamina and the medulla neuropils. In
262 control adult OLs (Figure 2E schematic), R-cell axons from the posterior edge of the
263 eye enter through the posterior lamina where R1-6 stop. R7 and R8 axons traverse the
264 outer optic chiasm and project into the anterior-most medulla; similarly, R-cell axons
265 from the anterior region of the eye project into the posterior medulla. All R7 and R8
266 axons enter the medulla neuropil from its distal face and their projections align in a
267 stereotyped array forming a retinotopic map (Figure 2E).
268
269 Analysis of *ClC-a* mutant adult OLs using a pan photoreceptor marker revealed
270 photoreceptor guidance defects. The guidance phenotypes observed could be classified
271 into three levels of severity based on the proportion of R-cell axons affected (Figure
272 2F). In brains with phenotypes classified as medium, a significant portion of posterior
273 R-cell axons bypassed the outer chiasm, projected along the posterior edge of the
274 medulla neuropil turning anteriorly, and extended for variable distances before
275 innervating the medulla neuropil from its proximal face. In many cases, this resulted in
276 posterior misplacement of the lamina neuropil. Despite the presence of these discreet
277 bundles of misprojected axons that originate posteriorly, the photoreceptor array was
278 maintained and mostly regular. We classified instances of few misprojected posterior
279 axons as weak phenotypes. Strong phenotypes were characterized by severe disruption
280 of the photoreceptor array and a posteriorly located, disorganized lamina. Despite the

281 difficulty in identifying discreet bundles of photoreceptor axons, distal innervation was
282 evident. These three degrees of severity showed variable penetrance and expressivity
283 depending on the allelic combination analyzed (Figure 2G). This variability could be
284 explained by the fact that *ClC-a* mutants were not complete nulls. A detailed analysis of
285 mutant photoreceptors also revealed layer selection defects for R8 and R1-R6 neurons
286 (Supplementary Figure 4A-J).
287
288 In order to confirm the requirement of *ClC-a* in glia, we performed cell-type-specific
289 knock down and rescue experiments. In addition to the *ClC-a* driver, we also used the
290 general glial driver Repo-GAL4 as an alternative to restrict transgene expression
291 selectively to glia. Using these two drivers, *ClC-a* knockdown by RNAi phenocopied
292 the photoreceptor phenotypes seen in the mutant (Figure 2H). Moreover, expression
293 with both glial drivers of *ClC-a* and rat *CLCN2* cDNA rescued the photoreceptor
294 phenotypes in whole mutant animals (Figure 2I). Although it has been suggested that
295 pupal photoreceptors express *ClC-a* (Ugarte et al., 2005), we did not observe this in
296 larval, pupal, or adult stages with the antibodies (data not shown) or reporters used in
297 this study (Supplementary Figure 2D-G). In addition, the absence of phenotype when
298 knocking down *ClC-a* in the eye disc or generating a full eye mutant for *ClC-a* (EGUF-
299 hid approach, data not shown), together with the inability to rescue the guidance
300 phenotype when expressing *ClC-a* in photoreceptors (Supplementary Figure 4K),
301 confirmed that *ClC-a* was required in glia for photoreceptor guidance.
302
303 Remarkably, taking advantage of the $05423^{ClC\text{-}a\text{-}GAL4}$ allele, we observed a rescue of
304 both OL size and photoreceptor guidance phenotypes in $05423^{ClC\text{-}a\text{-}GAL4}/Df$, the
305 strongest allelic combination, with *ClC-a* and *CLCN2* cDNA transgenes alike (Figure

306 2D, I). This finding indicated that brain size reduction and photoreceptor guidance
307 phenotypes in *ClC-a* mutants are non-autonomous and dependent on chloride channel
308 expression in glia, and that the fly and rat channels have equivalent functions.
309
310 **Expression of *ClC-a* in cortex glia is required for neuroepithelial expansion and**
311 **neuroblast divisions, and is sufficient to restore brain size.**
312 In order to unravel how mutations in *ClC-a* resulted in smaller brains, we first assessed
313 the status of glia in *ClC-a* mutants. We used the $05423^{ClC\text{-}a\text{-}GAL4}/14007$ allelic
314 combination to visualize glia membranes and nuclei in the mutant background. Our
315 analysis showed that the distribution pattern of glial cell bodies on the brain surface and
316 deep in the cortex was similar in control and mutant animals. Although the number of
317 nuclei/hemisphere volume ratio in the mutant was slightly reduced compared to control
318 (Supplementary Figure 5A), importantly, the membrane scaffold appeared
319 indistinguishable from the one observed in controls covering the whole hemisphere. As
320 in control animals, *ClC-a* mutant cortex glia processes were in close contact with the
321 OPC and IPC neuroepithelia (Figure 3A, B, E, F). In addition, in the OL and the CB
322 alike, cortex glia processes formed the trophospongium. Thus, individual neuroblasts
323 were enclosed in chambers that enlarged to adapt to their lineage expansion (Figure 3C,
324 G), and mature neuronal cell bodies were progressively enwrapped by cortex glia
325 processes (Figure 3D, D', H, H'). From these observations, we conclude that mutations
326 in the channel do not result in major morphological changes in the trophospongium
327 formed by cortex glia.
328
329 In turn, these results suggested that *ClC-a* was instead required for the proper
330 physiology of cortex glia. Cortex glia have been shown to be essential for neurogenesis

331 (Dumstrei et al., 2003), and since cortex glia processes are tightly associated with the
332 OPC (surface associated cortex glia (Morante et al., 2013)) and IPC, we set out to
333 examine whether the small OLs in mutant adult brain (Figure 2C) were a consequence
334 of defects in these neuroepithelia. Neuroepithelia in the OL start as sheets of cells that
335 divide symmetrically and expand until mid L3 (Ngo et al., 2010). As they do so, they
336 bend along the dorso-ventral axis, creating a crescent shaped structure with the opening
337 pointing posteriorly (Nassif et al., 2003). Already in late L2, while the OPC is still
338 growing to expand the pool of prospective neuroblasts, neuroepithelium to neuroblast
339 transition starts taking place. The lateral edge gives rise to LPC and the medial edge to
340 neuroblasts that will produce medulla neurons and glia (Egger et al., 2007, 2010; Ngo et
341 al., 2010; Orihara-Ono et al., 2011; Reddy et al., 2010; Wang et al., 2011a, 2011b;
342 Weng et al., 2012; Yasugi et al., 2010, 2008). Once neuroepithelium divisions stop and
343 the wave of differentiation continues, the OPC starts reducing in size and disappears in
344 early pupal stages, when it is all converted into precursors and neuroblasts. A similar
345 process takes place in the IPC, where different domains generate neuroblasts or
346 migrating progenitors (Apitz and Salecker, 2015; Hofbauer and Campos-Ortega, 1990)
347 until the neuroepithelium disappears.
348
349 We first checked if there were differences in neuroepithelia between control and mutant
350 animals. For this, we stained brains with the neuroepithelium marker E-cadherin and
351 manually segmented the tissue to generate a 3D reconstruction of these structures,
352 which yielded information about their morphology (Figure 4A) and size (Figure 4B). In
353 control animals in the mid L3 stage, the ends of the OPC and IPC crescents were close
354 together. In late L3, with the addition of progeny from neuroblasts, the OL was larger
355 and neuroepithelia crescents were wider and thinner. In comparison, in mid L3 mutant

356 animals, neuroepithelia maintained the same crescent shape as in controls but were
357 already clearly smaller (Figure 4B). By late L3, in most cases the OPC appeared as two
358 separate dorsal and ventral domains with the central part absent. Similarly, part of the
359 IPC was also missing (Figure 4A).
360
361 We next wondered whether the reduction in the size of the neuroepithelial sheets was
362 due to cell death. To test this idea, we stained larval brains with an antibody against the
363 apoptosis marker Dcp-1 (cleaved death caspase protein-1). Although developmental cell
364 death was taking place generally in the brain, we did not observe apoptotic cells either
365 in control or mutant neuroepithelial cells in mid or late L3 stages (Figure 4C). Thus, the
366 absence of cell death in this tissue suggested that defects in proliferation could be
367 responsible for the reduction in size of the OPC and IPC at mid L3, and also for the
368 morphological defects in late L3. In the latter, the lack of neuroepithelial cells in the
369 OPC central domain could be due to differentiation taking place (Supplementary Figure
370 6) in a neuroepithelium with reduced proliferation, which would result in a premature
371 disappearance of the tissue. To examine proliferation defects, we carried out a clonal
372 analysis study. With this technique, once mitotic recombination has been induced in a
373 dividing neuroepithelial cell, its progeny is labeled, and can thus be counted. Clones
374 were generated in the L2 stage and their size was assessed 48 hours later at mid L3.
375 Neuroepithelia clones generated in the control background (brains where cortex glia
376 expressed *ClC-a*) presented a median size of 21 cells for OPC clones and 14.5 cells for
377 IPC clones. Conversely, clones generated in the mutant background (brains where
378 cortex glia did not express *ClC-a*) were significantly reduced, with a median size of 9
379 and 8 cells for OPC and IPC clones, respectively (Figure 4D). Thus, *ClC-a* was
380 necessary in cortex glia for neuroepithelial expansion.

381

382 Given that *ClC-a* expressing cortex glia also cover the neuroblasts that originate from
383 the OPC as well as the neuroblasts in the CB, we also used clonal analysis to assess
384 neuroblast divisions in *ClC-a* mutants. The high density and proximity of neuroblasts
385 originating from the OPC renders it difficult to obtain single neuroblast clones
386 sufficiently apart from each other to be sure that the labeled progeny belongs to a single
387 neuroblast. Thus, we analyzed proliferation in neuroblasts from the CB since these are
388 sufficiently apart from each other. Importantly, both control and mutant animals showed
389 the same number of neuroblasts; thus, CB size reduction in mutants was not due to a
390 decrease in neuroblasts (Supplementary Figure 5B). Using the same clone induction
391 protocol as for neuroepithelial clones, the median size of type I neuroblast clones in the
392 control background was 34 cells, whereas the median size for clones in the mutant
393 background was reduced to 26 cells (Figure 4E). At this same mid L3 stage, we also
394 detected more cell death in mutant than control brains other than neuroepithelia, which
395 were death free (Figure 4F). This result suggested that alterations in the physiology of
396 cortex glia in *ClC-a* mutants affected the trophic role of cortex glia processes that wrap
397 the cell bodies of the more mature neurons of the lineage (Coutinho-Budd et al., 2017;
398 Dumstrei et al., 2003; Pereanu et al., 2005; Read, 2018; Spéder and Brand, 2018). Thus,
399 we cannot rule out the possibility that the reduction in neuroblast clone size could be
400 due to a combination of cell death and proliferation defects.

401

402 Together, these data suggest that the lack of *ClC-a* in cortex glia in the niche affects
403 neuroepithelial cell and neuroblast proliferation, as well as mature neuron viability
404 outside the niche. Consistent with both these observations, the size and growth rate of
405 larval hemispheres was reduced in the mutant background (Figure 4G). Thus, these

406 results are in accordance with a smaller OL (Figure 4H) and CB (Figure 4I) in adult
407 *ClC-a* mutant brains than in those of control flies. Importantly, expression of *ClC-a*
408 exclusively in cortex glia was sufficient to rescue the size of both structures in the adult
409 (Figure 4J, K).
410
411 **Defects are also observed in the neuroblast lineage that gives rise to ClC-a$^+$**
412 **ensheathing glia, which are necessary guideposts for photoreceptor axons**
413 **innervating the medulla**.
414 In an attempt to understand how the non-autonomous photoreceptor guidance
415 phenotype is related to *ClC-a* expression in the OL, we performed a detailed
416 developmental expression analysis in the region where photoreceptor innervation takes
417 place. In control L2 brains, horizontal views showed that the OPC and IPC were still
418 juxtaposed and that ClC-a$^+$ cell bodies were present on the surface of the brain and in
419 the CB (Figure 1D). In L3 frontal views, we observed that a population of glia, which
420 preceded the arrival of photoreceptor axons in the lamina (Dearborn, 2004; Perez and
421 Steller, 1996), progressively positioned amid the expanding region between the OPC
422 and IPC during the early to mid L3 stages (Figure 5A, B). This population was divided
423 into two sets of nuclei, the ClC-a$^-$ nuclei of satellite glia (Supplementary Figure 8A, B)
424 and a population of ClC-a$^+$ nuclei, with lower expression than cortex glia, which we
425 called boundary glia (Figure 5B). From this seemingly homogenous mid L3 boundary
426 glia population, two cell types could be distinguished in late L3 brains in frontal (Figure
427 5C) and horizontal views (Figure 5D, Supplementary Figure 8C): the Xg_o and a glial
428 type that has never been described before. We called these latter cells palisade glia (pag)
429 and they were positioned on the same plane as the cortex glia projection and the Xg_o,
430 forming a continuous glial barrier between the developing lamina and the LoP. We do

431 not know if pag persist or which type they are in the adult (Figure 5E). Xg_o are
432 considered tract-ensheathing glia, and one glial cell enwraps an average of 15 lamina-
433 medulla fiber tracts (Kremer et al., 2017). Two independent studies have shown that
434 Xg_o and Xg_i originate from the type II DL1 neuroblast lineage and migrate to the OL
435 (Ren et al., 2018; Viktorin et al., 2013). We repeated DL1 lineage-tracing experiments
436 and observed that progeny from the DL1 populated the OL following the same temporal
437 pattern as ClC-a^+ boundary glia (Supplementary Figure 8D-F). Hence, our data support
438 the idea that boundary glia are DL1 progeny that differentiate into the newly described
439 pag and Xg_o. Quantification of boundary glia in control brains showed that their
440 numbers increased from early to mid L3 and then dropped at late L3 (Figure 5M,
441 Supplementary Figure 8G, H). In mutant brains, however, we observed a striking
442 reduction in the number of boundary glial cells in mid and late L3 stages (Figure 5G-J,
443 M). Given that no glial apoptosis was observed in the region (Supplementary Figure 8I,
444 J), this result indicated that only very few boundary glia reached the OL in *ClC-a*
445 mutants.
446
447 To study the cause of this marked reduction, we first used the *earmuff* R09D11
448 genomic enhancer-fragment driven reporter CD4-tdtomato (Han et al., 2011) to
449 selectively label all type II neuroblast lineages and assess DL1. Type II neuroblast
450 lineages are characterized by the generation of intermediate neural progenitors (INP)
451 that can undergo several rounds of additional asymmetric divisions before they
452 disappear (Boone and Doe, 2008). In control brains, there are 8 type II neuroblasts, 6 of
453 which are positioned medially (DM1-6) and 2 laterally (DL1/2), closer to the OL
454 (Figure 5N, O). In mutants, although we observed some brains with instances of DM
455 mispositioning, the DL1/2 cluster was found together and laterally located with respect

456 to the rest of the DM neuroblasts (Figure 5P, Q). However, its position with respect to
457 the OL was sometimes changed. To assess proliferation defects in the lineage, our initial
458 approach was to compare control to mutant DL1 clones. However, even though the
459 clonal analysis protocol used in our study was very similar to those employed in other
460 studies analyzing type II clones, which are identified by the presence of INPs (Dpn
461 positive cells in the lineage), we obtained hardly any type II clones (2 out of 116
462 analyzed clones) and none in the DL1/2 cluster. As an alternative, we reasoned that we
463 could use the number of INPs in a lineage as readout for proliferation (Figure 5R).
464 Since DL1 and DL2 secondary axon tracts are extremely similar, we differentiated the
465 two lineages through expression of *gcm-LacZ* in the DL2 lineage (Viktorin et al., 2013)
466 (Supplementary Figure 9A), which consistently contained fewer INPs than DL1
467 (Supplementary Figure 9B). A comparison between control and mutant revealed that
468 both DL1 and DL2 lineages contained a higher number of INPs in the mutant condition
469 (Figure 5S-U). Given that we also observed proliferation defects in neuroepithelial
470 sheets and neuroblasts, it is reasonable to suppose that one of the reasons for the marked
471 reduction in boundary glia in mutants could be a reduced proliferation and hence
472 accumulation of DL1 INPs. Besides proliferation defects, it is also possible that
473 migration defects contribute to the marked reduction in boundary glia in mutant OLs.
474 Given that the DL1/2 cluster was found at different relative positions with respect to the
475 OL, and that the IPC, which is the region where these cells enter the OL in normal
476 conditions, is defective in mutants, boundary glia may be hindered from reaching their
477 final destination.
478
479 At this point, the question arises of how the marked reduction in boundary glia affects
480 photoreceptor guidance. Since the presence of boundary glia in mid L3 coincides with

481 the beginning of photoreceptor innervation, we next explored the spatiotemporal
482 relationship between these two cell types in control flies. As rows of ommatidia form in
483 the eye disc, photoreceptors extend axons that reach the OL through the optic stalk. In
484 mid L3 stages, R8s from the first rows of ommatidia projected into the posterior part of
485 the LPC field and their axons were located very close to boundary glia as they
486 continued to the medulla (Figure 6A, B). Photoreceptor innervation coincided with
487 cellular rearrangements, when boundary glia started to separate into pag and Xg_o glia.
488 Thus, in slightly older brains, R1-6 axons stopped and formed the lamina plexus above
489 the boundary glia cells that would become Xg_o, and R8 axons traversed the outer optic
490 chiasm, passing very close to the Xg_o (Figure 6C, D) and continued to the medulla,
491 innervating it through its distal face (Figure 5F). Hence, photoreceptors are in close
492 proximity to pag and Xg_o. Conversely, in mutant brains, the marked reduction in
493 boundary glia, and consequently in Xg_o, caused posterior R8 axons to skip the outer
494 chiasm and innervate the medulla from its proximal face (Figure 5L). The severity of
495 initial photoreceptor guidance errors determined the strength of the adult guidance
496 phenotypes. Consistent with Xg_o and Xg_i originating from DL1, in *ClC-a* mutants
497 chiasms did not properly form, which resulted in altered positioning of OL neuropils in
498 the adult brain (compare Figure 5E with Figure 5K).
499
500 Developmental guidance defects and adult outcomes of *ClC-a* mutants are both
501 extremely similar to OL specific *slit* mutants (Figure 6E-H) and *robo3* mutants (Pappu
502 et al., 2011; Tayler et al., 2004). The secreted chemorepellent molecule Slit and the
503 Robo family of receptors (Robo, Robo2, Robo3) have been implicated in preventing
504 photoreceptor axons from mixing with distal neuron axons from the LoP during
505 development, hence maintaining compartmentalization of this region of the developing

506 brain (Tayler et al., 2004). While receptors have been shown to be required in neurons,
507 *slit* reporters suggest that Slit protein in the region could be contributed by Xg_o (Pappu
508 et al., 2011; Tayler et al., 2004). A detailed developmental analysis of glial barrier
509 assembly allowed us to unequivocally characterize the temporal and cellular expression
510 pattern of *slit* with respect to photoreceptor innervation. To this end, we characterized
511 and used a MiMIC-based protein trap line for Slit (Supplementary Information,
512 Supplementary Figure 10). Our analysis indicated that Slit was already being expressed
513 in boundary glia in mid L3 (Figure 6I-K), when photoreceptors innervate the brain and
514 their axons come into close proximity with these glial cells. Moreover, removal of one
515 copy of *slit* enhanced the *ClC-a* photoreceptor guidance phenotype, suggesting a genetic
516 interaction between these two genes (Figure 6L), while knocking down *slit* in ClC-a^+
517 glia in the barrier recapitulated photoreceptor guidance defects (Figure 6M).
518
519 Based on our present results and previously published studies (Fan et al., 2005; Pappu et
520 al., 2011; Suzuki et al., 2016; Tayler et al., 2004), we propose that the substantial
521 reduction in boundary glia is most probably due to a combination of proliferation and
522 migration defects, which results in a significant reduction in Slit protein in the region.
523 As a consequence, photoreceptors that innervate the OL close to the glial boundary
524 fasciculate with the axons of neurons in the LoP known to innervate the medulla from
525 its proximal site.
526
527 **Expression of *ClC-a* exclusively in cortex glia is sufficient to restore ensheathing**
528 **glia guidepost cells and rescue photoreceptor guidance defects.**
529 To test whether *ClC-a* expression in cortex glia was sufficient to regulate DL1
530 proliferation, and assess if *ClC-a* expression in boundary glia (cell type classified as

531 ensheathing glia) played any role in photoreceptor guidance, we performed a cell-type-
532 specific rescue experiment. Because no reporter has yet been described that exclusively
533 labels boundary glia before photoreceptor innervation, we carried out a cortex glia-
534 specific rescue. We reasoned that with a cortex glia-specific driver, we could rescue the
535 generation of boundary glia from DL1 and at the same time avoid *ClC-a* expression in
536 boundary glia (Figure 7A). Since we could not specifically label boundary glia in this
537 experiment, we used Repo to mark and count glial nuclei in the region in mid L3, when
538 the first photoreceptors begin to innervate the brain. At this time, the glial population is
539 compact and easy to identify, whereas in late L3, additional ClC-a$^-$ glia such as
540 epithelial and marginal glia appear in high numbers and complicate counting. In control
541 animals, mid L3 glia nuclei included ClC-a$^-$ satellite glia and boundary glia (Figure 7A,
542 B). In mutants, the number of glial cells was reduced to half due to the marked
543 reduction in boundary glial cells (Figure 7A, B), but expression of *ClC-a* exclusively in
544 cortex glia resulted in an almost complete rescue in the number of glial cells present in
545 the barrier region in mid L3 (Figure 7A, B). More importantly, this boundary glia rescue
546 also rescued the photoreceptor guidance phenotype (Figure 7C). Surprisingly,
547 autonomous *ClC-a* expression in boundary glia was not necessary for their viability, for
548 migration from their point of origin in the CB to position themselves in the OL, or for
549 Slit secretion, since photoreceptor guidance defects were fully rescued when boundary
550 glia were in their position but did not express *ClC-a.* Thus, we conclude that the strong
551 reduction in boundary glia and the photoreceptor guidance phenotypes are a secondary
552 consequence of the *ClC-a* requirement in cortex glia and its function in neuroblast
553 proliferation.
554
555 **Mutations in *ClC-a* result in widespread wiring defects.**

556 Although we have characterized the origin of the guidance defects seen in
557 photoreceptors, wiring defects are not restricted to this cell type. The position and
558 morphology of neuropils in the visual system of *ClC-a* animals indicate that the wiring
559 of many other neurons in this system is also probably affected (compare Figure 5E to
560 K). Moreover, we also observed defects in CB structures such as mushroom bodies
561 (MBs). Each hemisphere contains one MB, which is formed by the neurons derived
562 from four special type I neuroblasts that never enter quiescence. These neurons extend
563 dendrites forming the calyx, and axons project into a fascicle called the peduncle that
564 splits into two branches called lobes (Figure 8A). Similar to photoreceptors, mushroom
565 bodies are neural structures that are highly dependent on glia-neuron interactions. It has
566 been shown that glia wrap the peduncle and the lobes during development (Spindler et
567 al., 2009) and in the adult (Kremer et al., 2017), and that different type II DM
568 neuroblasts contribute glia that associate with the mushroom body (Ren et al., 2018). In
569 control animals, ClC-a^{+} glia surrounded the MB calyx (Figure 8B) and the peduncle
570 (Figure 8D). Newly differentiated, FasII^{-} neurons projected their axons through the
571 center of the peduncle, generating a ring-like FasII^{+} pattern labeling the oldest neurons
572 (Figure 8C). In *ClC-a* mutant animals, axons often misprojected into the calyx (Figure
573 8F) and FasII staining filled the center of the peduncle, suggesting that newly generated
574 axons did not project through the center of this structure (Figure 8G). In addition, the
575 peduncle was much thinner (Figure 8G), although it seemed that ClC-a^{+} glia continued
576 to surround it. Comparison of control and mutant brains stained with antibody against
577 N-cadherin, which labels neuropils, revealed that the calyx, which in controls appeared
578 deep in the brain (Figure 8E), was more superficial in mutants (Figure 8I). MB clones
579 (Figure 8J) confirmed defects in the calyx and the peduncle (compare Figure 8K-M and
580 O). In MB clones in the control background, axons from the clone stayed together in a

581 bundle and extended into the center of the peduncle (Figure 8L). In instances where MB
582 clones in the mutant background extended axons into the peduncle (Figure 8M), these
583 axons defasciculated and projected into the peduncle through its periphery, leaving
584 older axons in the center (Figure 8N). In clones with strong phenotypes, almost all
585 axons terminated in the calyx and the peduncle was barely visible (Figure 8M).
586 Interestingly, these defects are very similar to those observed when cortex glia and
587 neuropil glia are eliminated: abnormal mushroom body morphologies including
588 splaying of axons and misguidance, and a misshapen superficial calyx due to premature
589 fusion of the four MB lineages in the cortical region (Spindler et al., 2009). Thus, as
590 observed for photoreceptor guidance phenotypes, MB defects in *ClC-a* mutants may be
591 due to reduced production of glia associated with MB circuitry, whether that glia is
592 ClC-a^{+} or not. In summary, since guidance defects in the *ClC-a* mutant seem to be
593 widespread, we propose that the *ClC-a* requirement for proper circuit assembly is not
594 restricted to the OL but is general to the brain.
595
596 **DISCUSSION**
597 In this study, we have shown that the *ClC-a* chloride channel function in the glial niche
598 has a non-autonomous but profound effect on two key aspects of neural development:
599 the generation of neurons and glia in the appropriate numbers, time, and place through
600 its role in regulating the proliferation of neurogenic tissues, and in consequence, the
601 correct assembly of neural circuits. Importantly, the fact that the fly (ClC-a) and rat
602 (CLC-2) chloride channels rescue brain size and guidance defects suggests that both can
603 perform the same physiological function. Concomitant defects in neuroblast
604 proliferation and photoreceptor targeting have been observed in other studies (González
605 et al., 1989; Kanai et al., 2018; Zhu et al., 2008), and it has been proposed that the

606 Activin signaling pathway is required to produce the proper number of neurons to
607 enable proper connection of incoming photoreceptor axons to their targets (Zhu et al.,
608 2008). Interestingly, mutations in the proneural gene *asense*, which is expressed in type
609 I neuroblasts and INPs, has adult targeting phenotypes that are extremely similar to the
610 ones observed in *ClC-a* mutants (González et al., 1989). Along the same lines, our study
611 links *ClC-a* photoreceptor guidance phenotypes to INP proliferation defects, and
612 furthermore identifies the INP-derived cellular population required for proper
613 photoreceptor axon guidance.
614
615 In addition to leukoencephalopathy, patients with mutations in *CLCN2* or altered
616 function of the channel also show cognitive impairment. Similarly *CLCN2* mutant mice
617 develop widespread vacuolization that progresses with age, but besides photoreceptor
618 and male germ cell degeneration, they do not display immediately visible behavioral
619 defects (Blanz et al., 2007; Bösl et al., 2001; Edwards et al., 2010). However, *CLCN2* is
620 expressed in astrocytes and oligodendrocytes early in development (Makara et al., 2003)
621 and has been detected in Bergman glia (Jeworutzki et al., 2012), which are important for
622 neuronal migration in the formation of cortical structures. Together with our findings,
623 these observations suggest that it would be worth exploring the role of this channel in
624 the vertebrate neural stem cell niche. Interestingly, expression of *CLCN2* has been
625 found outside the brain in an unrelated stem cell niche. It is expressed in Sertoli cells
626 (Bösl et al., 2001), which are the primary somatic cells of the seminiferous epithelium
627 that form the spermatogonial stem cell niche through physical support and expression of
628 paracrine factors (Chen et al., 2005; Oatley et al., 2011). *CLCN2* mutant mice showed
629 disorganized distribution of germ cells in tubules at 3 weeks, germ cells did not pass
630 beyond meiosis I, and were completely lost at later stages (Bösl et al., 2001; Edwards et

631 al., 2010). Hence, similarly to ClC-a regulation of proliferation in the neural stem cell
632 niche, CLC-2 could be regulating proliferation in the spermatogonial stem cell niche.
633
634 Although the Sertoli *CLCN2* expression/germ cell depletion correlation in mouse is in
635 accordance with our data suggesting an important role of the ClC-a/CLC-2 chloride
636 channel in stem cell niches, it remains unclear how a chloride ion channel could non-
637 autonomously modulate the mitotic activity of proliferative cells. ClC-a function in
638 Malpighian tubules has been associated with the movement of Cl^- ions (Cabrero et al.,
639 2014), but it is possible that its function in glia of the stem cell niche is unrelated to ion
640 exchange. For example, it might recruit signaling molecules to modulate neuroblast
641 proliferation. Conceptually, one way to test whether the channel function is related to
642 the movement of ions would be to perform rescue experiments of *ClC-a* mutant
643 phenotypes with a channel defective for the pore function. In practice, however, this
644 type of experiment is not that straightforward since CLC-2 pore gating is quite complex.
645 Channels of the CLC family are thought to function as a homodimers, with each subunit
646 forming a pore and presenting both independent and common pore gating mechanisms
647 (Jentsch and Pusch, 2018). Given the many studies supporting the function of CLC-2 as
648 a channel, we next discuss different ways in which ionic imbalance caused by mutations
649 in *ClC-a* could result in the phenotypes described. One of the possibilities we
650 considered was whether ionic imbalance in *ClC-a* mutants affected secretion. Glial
651 cells secrete different types of factor to the extracellular space, both during development
652 and to maintain morphology in the adult (Coutinho-Budd et al., 2017; Read, 2018;
653 Spéder and Brand, 2018). In the niche in particular, there are several examples of glia-
654 secreted molecules that regulate neurogenic proliferation, such as the transforming
655 growth factor a (TGF-a)-like ligand (Morante et al., 2013) and insulin-like peptides

656 (dILPs) (Chell and Brand, 2010; Sousa-Nunes et al., 2011). In vertebrates, an increase
657 in intracellular Ca^{2+} in astrocytes, which is caused by activation of G protein–coupled
658 receptors and release of calcium from intracellular stores or calcium entry from the
659 extracellular space through different types of channel, has been reported to evoke the
660 release of gliotransmitters (Bazargani and Attwell, 2016; Khakh and McCarthy, 2015;
661 Shigetomi et al., 2016). In this scenario, membrane potential changes mediated by Cl^-
662 channel activity could modulate activation of GPCR or voltage dependent Ca^{2+}
663 channels, mediating an increase in the Ca^{2+} intracellular concentration and resulting in
664 secretion. In fact, the opening of voltage dependent Ca^{2+} channels has been proposed as
665 the mechanism behind the increase in aldosterone production and secretion (Fernandes-
666 Rosa et al., 2018) resulting from gain-of-function mutations of *CLCN2*, which are
667 behind primary aldosteronism and cause sustained depolarization of glomerulosa
668 adrenal cells (Fernandes-Rosa et al., 2018; Scholl et al., 2018). To test whether loss of
669 function of ClC-a/CLC-2 channels also affected secretion, we performed glia-specific
670 RNAi knock down of key upstream regulators of intracellular calcium release such as
671 *Drosophila* IP3R and RyR receptors, and downstream effectors of calcium-regulated
672 secretory vesicle exocytosis, as well as secretion assays in primary glial cultures where
673 *CLCN2* was knocked down with RNAi (data not shown). However, we were unable to
674 consistently recapitulate *ClC-a* mutant phenotypes or detect secretion defects,
675 suggesting that if the absence or reduction of the channel impairs secretion, it does so
676 only in a very limited way.
677
678 Another possibility is that ClC-a is involved in pH regulation. Under extracellular
679 neutral pH, H^+ and HCO_3^- combine to form H_2CO_3, which in turn is in equilibrium with
680 H_2O and CO_2. In acidic conditions, to compensate for the increase in H^+, the HCO_3^-/Cl^-

681 exchangers extrude HCO_3^- to the extracellular space to form more H_2CO_3 and drive the
682 reaction to the formation of H_2O and CO_2. Rat ClC-2 opens in response to extracellular
683 acidification, allowing Cl^- to exit the cell (Jordt and Jentsch, 1997). Since for each
684 molecule of HCO_3^- extruded, one of Cl^- is internalized, ClC-2 activation might be
685 required to regulate HCO_3^- transport and allow the presence of extracellular Cl^-, thus
686 creating a Cl^- recycling pathway for HCO_3^-/Cl^- exchangers (Bösl et al., 2001). Assays in
687 *Xenopus* oocytes have shown that ClC-a activity is also sensitive to pH (H. G-P. and R.
688 E., unpublished results). Thus, it may be that the lack of ClC-a in cortex glia leads to a
689 more acidic extracellular pH due to deficient Cl^- recycling for HCO_3^-/Cl^- exchangers.
690 Since changes in extracellular and intracellular pH have been shown to affect the
691 proliferative capacity of both wild type and cancer cells (Carswell and Papoutsakis,
692 2000; Ciapa and Philippe, 2013; Flinck et al., 2018; Persi et al., 2018; White et al.,
693 2017), ClC-a function in pH regulation could explain the proliferation defects observed
694 in the mutant.

695

696 Regardless of the molecular mechanism that mediates the effect of ClC-a on
697 proliferation, our findings support the notion that glia-mediated ionic balance could be
698 important for brain development. Our results are in accordance with those of recent
699 studies suggesting a link between several ion channels and the development of the
700 nervous system, with channels being important both in stem cells (Li, 2011; Liebau et
701 al., 2013) and glia (Olsen et al., 2015). A recent example of a channel function in stem
702 cells is the gene SCN3A, which codes for the NaV1.3 sodium channel. This channel is
703 mainly expressed during development and is highly enriched in basal/outer radial glia
704 progenitors and migrating newborn neurons (Smith et al., 2018). The appearance of this
705 type of progenitor and defined neuronal migration has been associated with the

706 establishment of gyri in the cortex (Fietz et al., 2010; Hansen et al., 2010; Reillo et al.,
707 2011). Intriguingly, mutations in the SCN3A gene result in structural malformations of
708 gyri in the cortex (Smith et al., 2018). Another example is the glial-specific Kir4.1
709 channel, which is related to neurodevelopmental disorders with associated cognitive
710 defects. Mutations in *KCNJ10*, which codes for the glial-specific Kir4.1 channel,
711 underlie SeSAME/EAST syndrome (seizures, sensorineural deafness, ataxia,
712 intellectual disability and electrolyte imbalance/epilepsy, ataxia, sensorineural deafness
713 and tubulopathy) (Bockenhauer et al., 2009; Scholl et al., 2009) and have been detected
714 in patients diagnosed with autism spectrum disorder and epilepsy (Sicca et al., 2016,
715 2011). Reduced Kir4.1 expression in astrocytes significantly contributes to the etiology
716 of Rett syndrome (Kahanovitch et al., 2018; Lioy et al., 2011), which shares many
717 pathophysiological traits with SeSAME/EAST. Moreover, Kir4.1 protein is detected as
718 early as embryonic day 20 in glial cells in the developing cortex and hippocampus
719 (Moroni et al., 2015), suggesting that it could influence neural development in these
720 regions. Together with our findings, these observations suggest that mutations in ion
721 channels could affect neurogenesis and connectivity, resulting in intellectual disabilities.
722 Thus, providing insights into the developmental stages affected by impaired glial-
723 dependent homeostasis could help improve our understanding of the origin of the
724 cognitive deficiencies detected in patients with channelopathies or conditions where ion
725 channels in glia are not functional.
726

727 **MATERIALS AND METHODS**

728 **Genetics**

729 Flies were grown in standard medium at 25ºC except for RNAi experiments, which
730 were performed at 29ºC. All genotypes analyzed are specified in the Supplementary
731 Information.
732 Stocks used to characterize *ClC-a* expression and phenotype were: *MiMIC 05423*
733 (Bloomington Drosophila Stock Center, BDSC 43680), *05423*$^{ClC\text{-}a\text{-}GAL4}$ (BDSC 66801),
734 *MiMIC 14007* (BDSC 59247), *Df(3R)PS2* (BDSC 37742), *mir8-GAL4* (DGRC
735 104917), *R54H02-GAL4* (BDSC 45784), *wrapper932i-LexA*, *wrapper932i-GAL80*
736 (Coutinho-Budd et al., 2017), *repo-GAL4* on II (Lee and Jones, 2005), *repo-GAL4* on
737 III (BDSC 7415), UAS-Dcr2 (Vienna Drosophila Resource Center, VDRC 60009),
738 *UAS-ClC-a-RNAi* (VDRC 110394), *UAS-ClC-a* and *UAS-ClCN2* (this study), *UAS-slit-*
739 *RNAi* (VDRC 108853), *slit*^{dui} (BDSC 9284), *Slit-GFP* (BDSC 64472), and R9D11-
740 tdtom (BDSC 35847). Additional stocks used in Supplementary Figures were: *ClC-a-*
741 *GFP* (BDSC 59296), *slit-lacZ* (*Slit*^{05428}*)* (BDSC 12189), *Rh1GAL4* (BDSC 68385),
742 *Rh4EGFP* (BDSC 7462), *Rh6-lacZ* (BDSC 8117), *GMR-GAL4* (BDSC 1104), *R43H01-*
743 *LexA* (BDSC 47931) and *R25A01-GAL4* (BDSC 49102), *gcm-lacZ* (BDSC 5445).
744 To label membranes and nucleus, we used *UAS-mCD8-GFP* (BDSC 5137), *UAS-*
745 *mCD8-RFP.LG* (BDSC 27398), *UAS-mCD8GFP,lexAop-CD2RFP* (BDSC 67093),
746 *UAS-H2B-RFP* (Mayer et al., 2005), and *UAS-H2B-YFP* (Bellaïche et al., 2001), as
747 specified in the genotype list. In experiments where nuclear labeling was used for
748 quantification, the same transgene was employed for control and mutant samples (Fig
749 5M, Sup Fig 5A).
750 To generate and label neurogenic tissue clones in control and *ClC-a* mutant
751 backgrounds (Figure 4D,E and Figure 8J), the following stocks were crossed:
752 *hsFLP,FRT19A,tub-Gal80; tub-GAL4,UAS-mCD8GFP/CyODfYFP; 14007/+* to
753 *FRT19A; +; +* and *hsFLP,FRT19A, tub-Gal80; tub-GAL4,UAS-*

754 *mCD8GFP/CyODfYFP; 14007/+* to *FRT19A; +; Df(3R)PS2/TM6B*. Three-hour egg
755 lays were maintained at 25ºC and clone induction was performed with a 30-minute heat
756 shock pulse at 37ºC in a water bath at the L2 stage. Brains were dissected 48 hours after
757 clone induction.
758 For lineage-tracing experiments (Supplementary Figure 8D-F, G), we used G-TRACE
759 (*UAS-RedStinger,UAS-FLP,Ubi-FRT-stop-FRT-Stinger*, BDSC 28280 (Evans et al.,
760 2009) combined with specific *GAL4* drivers.
761 When we performed the cortex glia-specific rescue experiments (Figure 4J, K and
762 Figure 7B, C), no cortex glia-specific driver had yet been published, so we devised an
763 intersectional genetic strategy to generate one using the *mir8-GAL4* driver. In addition
764 to surface associated cortex glia on the OPC, *mir8-GAL4,* labels cortex glia and neurons
765 in the brain, as well as other cells in the animal. To restrict *mir-8* expression exclusively
766 to cortex glia, we combined the following transgenes: *repo-FLP6.2* (Stork et al., 2014),
767 *tub>GAL80>* (BDSC 38879), and *mir8-GAL4*. In this combination, GAL4 is only
768 expressed in cortex glia since the GAL80 repressor has only been flipped out in this cell
769 type but persists in non-glial mir-8 expressing cells (Supplementary Figure 7). For the
770 sake of simplicity, we refer to this combination as the *mir-8* ^{cxg} driver.
771
772 **DNA constructs**
773 For *UAS-ClC-a* and *UAS-CLCN2* transgenes, we used the Gateway cloning system
774 (Invitrogene) and cloned their respective cDNAs, to which a 3xFLAG tag had been
775 previously added in the C-terminus, into the ΦC31 integrase compatible pBID-UASC-G
776 plasmid (Addgene plasmid # 35202, a gift from Brian McCabe (Wang et al., 2012)).
777 The FLAG tag does not alter the electrophysiological properties of these channels. For
778 the *ClC-a* construct, we used the isoform C (a gift from P. Cid) since its

779 electrophysiological properties have already been studied in *Xenopus* oocytes and HEK-
780 293 cells (Flores et al., 2009; Jeworutzki et al., 2012), and it is known to be expressed in
781 *Drosophila* head and body (Flores et al., 2009). The final constructs were injected into
782 the *attp40* (25C6) landing site on the 2nd chromosome.
783
784 **Immunohistochemistry**
785 Fly brains were dissected in Schneider medium and fixed in 4% PFA in PBL (75 mM
786 lysine, 37 mM sodium phosphate buffer, pH 7.4) for 25 min. After fixation, the tissue
787 was washed in PBS with 0.5%Triton-X-100 (PBST) and blocked with PBST with 10%
788 normal goat serum. Primary and secondary antibody incubations were performed in
789 PBST and 10% normal goat serum, typically overnight at 4°C. The following primary
790 antibodies were used for immunohistochemistry: mouse anti-Chaoptin (1:50, 24B10,
791 Developmental Studies Hybridoma Bank, DSHB), rat anti-DE-cadherin (1:50, DCAD2,
792 DSHB), mouse anti-Repo (1:50, 8D12, DSHB), rabbit anti-ClC-a (1:100 this study, see
793 Supplementary Information, and 1:100 a gift from J. Dow), guinea pig anti-Deadpan
794 (1:2000, gift from A. Carmena), rat anti-Lethal of Scute (1:5000, gift from A. Brand),
795 rabbit anti-Mira (1:500, gift from C. González), chicken anti-GFP (1:800, ab13970,
796 Abcam, Cambridge, UK), rabbit anti-RFP (1:200, 632496, Clontech, Mountain View,
797 CA, USA), mouse anti-β-galactosidase (1:1000, Z3783, Promega, Madison, WI, USA),
798 rabbit anti-β-galactosidase (1:1000, 0855976, Cappel, Malvern, PA, USA), and rabbit
799 anti-Dcp-1 (1:200, Asp216, Cell Signaling Technology, Danvers, MA, USA). Alexa
800 Fluor 488, 568, and 647 secondary antibodies raised in rabbit, mouse, rat, guinea pig, or
801 chicken (Life Technologies, Carlsbad, CA, USA) were used at 1:250 concentration.
802 Nuclei were labeled using TOPRO-3 (1:1000, T3605, Life Technologies). Brains were
803 mounted for confocal microscopy in Vectashield (Vector Laboratories, Burlingame,

804 CA, USA). Samples were analyzed with Leica TCS SPE and Zeiss LSM880 confocal
805 microscopes.
806
807 **Photoreceptor phenotype classification**
808 We classified brains as having a strong, medium, or weak photoreceptor phenotype
809 based on the OL that out of the two had the most severe phenotype. If not the same, the
810 two OLs tended to be in consecutive categories (i.e. strong/medium, medium/weak,
811 weak/no phenotype). For experiments involving photoreceptor phenotypes, we always
812 analyzed at least 17 brains.
813
814 **Measurements and quantifications**
815 To assess adult OL and CB size, we took two confocal images of each brain in the
816 appropriate orientations to measure the antero-posterior and dorso-ventral axis of each
817 structure at their widest part. We multiplied those two measurements to obtain a relative
818 value in arbitrary units (a.u). The number of brains analyzed ranged from 23 to 44 for
819 OL (to obtain fully independent measurements, only one OL per brain was quantified),
820 and from 12 to 22 for CB when assessing phenotype (Figure 2C, Figure 4H, I). In
821 rescue experiments (Figure 2D, Figure 4J, K), the number of brains analyzed ranged
822 from 12 to 32.
823 To assess brain size at different larval stages (Figure 4G), the diameter of one larval
824 brain hemisphere per animal was measured in the antero-posterior axis. The *n* ranged
825 from 23 to 37 animals analyzed.
826 To quantify the number of cortex glia nuclei in late L3 OLs, we manually counted *ClC-*
827 a^+ nuclei (Supplementary Figure 5A). Cortex glia nuclei present an average size of
828 approximately 44.5 μm^2 (Morante et al., 2013) and are clearly distinguishable from

829 ClC-a$^+$ ensheathing glia nuclei by their size and position in the OL. The *n* for this
830 experiment was 8 brains.
831 To count the number of neuroblasts in the CB part of the hemisphere (Supplementary
832 Figure 5B), we manually identified them based on their nuclear size and on Dpn and
833 Mira antibody staining. Neuroblasts were distinguishable from mature INPs, which are
834 also Dpn$^+$ and Mira$^+$, by their smaller nuclear size and higher intensity of TOPRO-3
835 nuclear staining. The *n* for this experiment was 8 brains. To measure neuroepithelia
836 volume, the tissue was stained with anti-E-cadherin antibody and manually segmented
837 using the "SURFACE" tool included in Imaris software. This tool provides the volume
838 in μm^3 of the surfaces generated (Figure 4B). The *n* for this experiment was between 8
839 and 9 brains.
840 To quantify the number of cells in OPC, IPC, and CB neuroblast clones (Figure 4D, E),
841 we performed manual counting in confocal stacks. Cells in the clone were identified as
842 TOPRO+ nuclei surrounded by labeled membrane. We counted as many clones as
843 possible per brain provided that they were identifiable as individual clones. The number
844 of clones analyzed was 52 (control) and 31(mutant) in the OPC and 18 (control and
845 mutant) in the IPC, and the number of type I neuroblast clones was 39 (control) and 22
846 (mutant).
847 To assess cell death in developing OLs (Figure 4F), we manually counted Dcp-
848 1$^+$/TOPRO$^+$ puncta per brain hemisphere. This value was divided by the hemisphere
849 volume obtained through manual segmentation of the structure and using the
850 "SURFACE" tool included in Imaris software. The *n* for this experiment was 6 brains.
851 To quantify the subset of boundary glia among glial cells in the chiasm region at
852 different stages, we manually counted ClC-a$^+$/Repo$^+$ nuclei (Figure 5M). The *n* for this
853 experiment was 5 brains.

854 To quantify mature INPs in the DL1 and DL2 lineages (Figure 5U), we manually
855 counted Dpn$^+$ positive nuclei surrounded by tdtom$^+$ membranes of the *R9D11-tdtomato*
856 marker. To differentiate DL1 from DL2, we used *gcm-lacZ*, which specifically labels
857 the DL2 lineage (Supplementary Figure 9). The *n* for this experiment was between 11
858 and 12 brains.
859 To quantify the number of total glial cells in the future chiasm region in mid L3 (Figure
860 7B), we manually counted Repo$^+$ nuclei in confocal stacks. The *n* for this experiment
861 was between 5 and 8 brains.
862
863 **Image processing**
864 Fiji or Imaris 8.0 (Bitplane, South Windsor, CT, USA) were used to process confocal
865 data as specified in figure legends. Figures were assembled using Adobe Illustrator
866 (Adobe, San Jose, CA, USA).
867
868 **Statistics**
869 Statistical analysis was carried out using Prism 6 (GraphPad Software Inc, San Diego,
870 CA, USA). When data did not follow a normal distribution or resulted from a previous
871 mathematical computation (i.e. ratio to volume), we used non-parametric tests. For
872 group comparisons, we used Kruskal-Wallis followed by planned pairwise comparisons
873 with the Mann-Whitney post hoc test to obtain *p*-values (Figure 2C, D; Figure 4B, H, I;
874 Figure 5M; Figure 7B; Supplementary Figure 8H). For pairwise comparisons, we used
875 Mann-Whitney's test (Figure 4D, E, F, J, K, Figure 5U, Supplementary Figure 9B). For
876 paired comparisons, we used the Wilcoxon matched-pairs squad rank test (Figure 5U).
877 Data are shown in box plots where the median is given between the first and third
878 quartiles. Whiskers represent the maximum and minimum values of the data. When all

879 data in the analysis were suitable for a parametric analysis, we performed one-way
880 ANOVA followed by Turkey's post hoc test to obtain *p*-values (Figure 4G). *p*-values
881 for pairwise comparisons relevant to our biological inquiry are shown in the bar graph.
882 Data is represented as the mean, and error bars show standard deviation.
883 To evaluate the statistical significance of enhancements in qualitatively categorized
884 photoreceptor phenotypes (i.e., strong, medium, weak, no phenotype) (Figure 6L, M),
885 we performed a Chi-squared test of independence between phenotype categories and
886 genotypes to obtain *p*-values.
887

888 **ACKNOWLEDGMENTS**

889 We are grateful to A. Brand, H. Bellen, A. Carmena, P. Cid, J. Coutinho-Budd, J.A.
890 Dow, M. Freeman, C. Gonzalez, B.W. Jones, C. Klambt, J. Morante, I. Salecker, M.
891 Wernet, DSHB, BDSC, and VDRC for reagents. We thank V. Hartenstein, J. Modolell,
892 C. González, A. Carmena, J. Tejedor, and C. Homem for helpful discussions and
893 suggestions on optic lobe and brain development. We thank F. Aguado, N. Barranco,
894 and X. Elorza-Vidal for performing secretion experiments in cell culture. We thank M.
895 Bosch from the Confocal Unit of the CCiT-UB. We thank F. Cebriá for critical reading
896 of the manuscript. Our gratitude to M. Corominas, F. Serras, and members of their
897 laboratories for engaging in discussions and making suggestions during our joint lab
898 meetings throughout the project. This work was funded in part by the Spanish Ministry
899 of Economy and Competitiveness through grants BFU2015-69689-P to M.M. and M.R,
900 and SAF2015-70377 to R.E.; the Generalitat de Catalunya through grant SGR2014-
901 1178 to R.E.; the Institució Catalana de Recerca i Estudis Avançats through an ICREA
902 Academia award to R.E.; and the University of Barcelona through the award of an APIF
903 fellowship to H.P-S.

904

905 **AUTHOR CONTRIBUTIONS**

906 M.M. and R.E. conceived the project; M.M., H.P-S., Q.Z., R.E., and H. G-P. designed
907 the experiments and data analysis; H. G-P. and R.E. contributed reagents and analytical
908 tools; M. R. designed the statistical analysis; H.P-S. and Q.Z. performed the
909 experiments; H.P-S., Q.Z, M.R., and M.M. analyzed the results; and M.M. wrote the
910 manuscript with contributions from all the other authors.

911

912 **FIGURE LEGENDS**

913 **Figure 1. *ClC-a* is expressed in cortex glia and ensheathing glia during brain**
914 **development.**

915 (A-I) Analysis of *ClC-a* expression in the developing brain. Brain illustrations show the
916 orientation of imaging planes for the indicated panels at different larval stages. *ClC-a*
917 specific GAL4 driver (*ClC-a-GAL4)* was used to label cellular membranes (green) and
918 nuclei (red) of ClC-a^{+} cells. Glial nuclei were labeled with anti-Repo antibody (blue).
919 Anti-E-cadherin (E-cad, magenta) was used to identify neuroepithelial cells.
920 Neuroblasts and photoreceptors were labeled with anti-Deadpan (Dpn, gray) and anti-
921 Chaoptin (24B10, gray), respectively. (A-B) Lateral view of L1 brain hemispheres
922 outlined with a dashed line. A' shows Repo staining from A. (C, D) Horizontal views of
923 L2 brain hemispheres. (E, F) Horizontal views at the surface of late L3 brain
924 hemispheres. Asterisks in E mark examples of cortex glia chambers. (G) Horizontal
925 view through the middle of the L3 brain hemisphere. The lamina furrow (LF) is the
926 indentation where OPC gives rise to LPCs in the lateral side. (H) Horizontal view at the
927 same level as G, showing the region demarcated by the dashed box in the schematic on
928 the right. Photoreceptors enter the brain through the LPC region. (I) Frontal view of a

929 volume-rendering 3D reconstruction of the OL corresponding to the region demarcated
930 by the dashed square in the schematic at the top. The membranes of ClC-a$^+$ glial nuclei
931 created a barrier that separated the developing lamina and the LoP. (J-Q) Identification
932 of ClC-a$^+$ glial types. (J-K) Characterization of ClC-a$^+$ cells on the OPC. (J) Analysis of
933 ClC-a$^+$ nuclear position with respect to the BBB. (K) Colocalization analysis of *ClC-a*
934 protein with *mir-8*. Expression in LF is marked by an arrow and expression between the
935 LPC and the LoP is marked by arrowheads. (L-N) Confirmation of *ClC-a* expression in
936 cortex glia. (L) Membrane and nuclear patterns obtained with the *wrapper* GAL4 driver
937 (*R54H02-GAL4)* For similarity to *ClC-a-GAL4* generated patterns, compare to panel G.
938 (M-N) Colocalization study of membrane patterns generated by the *ClC-a-GAL4* driver
939 and a *LexA* driver version of the cortex glia *wrapper* driver (*wrapper932i-LexA*) using
940 *UAS* and *lexAop* fluorescent reporters. (M) Horizontal view of the brain surface. To
941 visualize *ClC-a* expression (green) in the CB (dashed region of interest), gain had to be
942 elevated, with the consequent saturation of expression in the OL. M' and M" show *ClC-*
943 *a* (green) and *wrapper* expression (red), respectively, from the region of interest in M.
944 (N) Deeper section into the hemisphere imaged with gain conditions to analyze OL
945 colocalization; thus, the *ClC-a* signal (green) in the CB is very low. N' and N" show
946 *ClC-a* (green) and *wrapper* (red) membrane signals. (O-Q) Identification of non-cortex
947 glia ClC-a$^+$ cells as ensheathing glia. (O) *ClC-a* is expressed in neuropil-ensheathing
948 glia (eng) surrounding CB neuropils, and tract-ensheathing glia wrapping the mushroom
949 body peduncle (Pe, inset). (P) *ClC-a* is expressed in glia surrounding the mushroom
950 body calyx. (Q) *ClC-a* is expressed in palisade glia and in the outer chiasm glia (Xg_o),
951 which wraps photoreceptor axons in their transition from the lamina to the medulla
952 neuropils.

953 OPC, outer proliferation center; IPC, inner proliferation center; OL, optic lobe; CB,
954 central brain; LF, lamina furrow; LPC, lamina precursor cells; LoP, lobula plug; cxg,
955 cortex glia; sg, satellite glia; pag, palisade glia; eg, epithelial glia; mg, marginal glia;
956 Xg_o, outer chiasm glia; BBB, blood brain barrier; Pe, peduncle; egn, neuropil-
957 ensheathing glia; Ca, calyx. Scale bars represent 10 µm.
958 (See also Supplementary Figures 1 and 2)
959
960 **Figure 2. *ClC-a* mutants have smaller brains and photoreceptor guidance defects.**
961 (A) Schematic of *ClC-a* transcripts in the *ClC-a* locus and the insertion location of
962 *Mi(MIC)ClC-a*^{05423} and *Mi(MIC)ClC-a*^{14007} transposons. (B) Magnification of the pink
963 dashed box around *Mi(MIC)ClC-a*^{05423} in A. The original *Mi(MIC)* transposon cassette
964 contains a splice acceptor followed by stop codons in all reading frames, followed by
965 the EGFP coding sequence with a polyadenylation signal. When inserted in an intron
966 between coding exons in the orientation of gene transcription, use of the transposon's
967 splice acceptor generates truncated transcripts. The Trojan-GAL4 cassette swapped with
968 RMCE to generate *05423*$^{ClC\text{-}a\text{-}GAL4}$ contains a splice acceptor that ensures the T2A-
969 GAL4 open reading frame is included in the mRNA of the *ClC-a* gene. The T2A
970 sequence promotes separate translation of GAL4. (C-D) Quantification of OL size in
971 arbitrary units. *p*-values were calculated with the non-parametric Mann-Whitney test.
972 (C) Comparison of OL size of two *ClC-a* mutant allelic combinations, *05423*$^{ClC\text{-}a\text{-}}$
973 ^{GAL4}*/14007* and *05423*$^{ClC\text{-}a\text{-}GAL4}$*/Df,* and their respective controls. (D) Comparison of OL
974 size of *05423*$^{ClC\text{-}a\text{-}GAL4}$*/Df* and mutant brains in which *ClC-a (UAS-ClC-a)* or rat *CLCN2*
975 (*UAS-CLCN2*) mRNAs were expressed in glia. (E-I) Characterization of photoreceptor
976 guidance defects. (E) Confocal section of an adult OL of a heterozygous control animal
977 (*14007/+*), showing the wild type photoreceptor array stained with anti-Chaoptin

978 (24B10, green). The schematic shows the trajectory of R7 and R8 photoreceptor axons.
979 (F) Confocal images of adult OLs from the *14007/Df* mutant allelic combination
980 classified according to phenotype severity. For the sake of simplicity, the schematic
981 depicts the altered trajectory of R7 and R8 axons of a single ommatidium. To show the
982 complete trajectory of misguided photoreceptors, images for the weak and medium
983 phenotypes are Z-projections of confocal stacks. (G-I) Photoreceptor phenotype
984 analysis for different experiments. Phenotype penetrance and expressivity for each
985 condition is depicted as the percentage of brains with no phenotype, weak, medium, and
986 strong phenotypes (see Material and Methods). Heterozygous controls in (G) and (H)
987 show no phenotype. (G) Classification of *ClC-a* mutant allelic combinations according
988 to strength of their penetrance and expressivity. (H) Analysis of glia-specific knock
989 down of *ClC-a* using RNAi. (I) Glia-specific rescue experiment using *ClC-a* and rat
990 *CLCN2* mRNAs in two allelic combinations, *14007/Df* and $05423^{ClC\text{-}a\text{-}GAL4}/Df$.
991 Scale bars represent 10 µm. ** $p<0.01$, *** $p<0.001$.
992 (See also Supplementary Figures 3 and 4)
993
994 **Figure 3. The cortex glia membrane scaffold remains unaltered in *ClC-a* mutant**
995 **animals.**
996 Analysis of cortex glia membrane scaffold (green) and nuclear (red) distribution in
997 control ($05423^{ClC\text{-}a\text{-}GAL4}/+$) and mutant ($05423^{ClC\text{-}a\text{-}GAL4}/14007$) brain hemispheres.
998 Horizontal views at specified developmental times and depths are shown. (A, B) View
999 through the middle of the early (A) and late (B) L3 hemisphere of a control animal.
1000 Anti-E-cadherin (E-cad, magenta) labels neuroepithelial cells. (C) View of the surface
1001 of a control brain stained with anti-Deadpan (Dpn, gray) to visualize neuroblasts. (D,
1002 D') Slightly deeper view of the surface of a control brain stained with anti-Elav to

1003 visualize postmitotic neurons. (E), (F), (G) and (H, H') panels are equivalent views and
1004 stainings in mutant animals.
1005 OPC, outer proliferation center; IPC, inner proliferation center. Scale bars represent 10
1006 μm.
1007 (See also Supplementary Figure 5)
1008
1009 **Figure 4. *ClC-a* is required for neuroepithelial cell and neuroblast proliferation, as**
1010 **well as neuronal viability, and is sufficient to rescue brain size.**
1011 *p*-values of indicated comparisons were calculated with the non-parametric Mann-
1012 Whitney test unless otherwise indicated. (A) Images of surface-rendering 3D
1013 reconstructions of the OPC (magenta) and IPC (cyan) shown from lateral and posterior
1014 views, in control (*14007/+*) and mutant (*14007/Df)* brains. Bracket indicates the
1015 absence of the central domain of the OPC in mutant late L3 reconstructions. (B)
1016 Quantification and comparison of the volume in μm^3 of reconstructed OPC (magenta)
1017 and IPC (cyan) of mid and late control and mutant animals. (C) Analysis of cell death in
1018 mid L3 OPC and IPC (E-cad, gray) of control and mutant animals using anti-Dcp-1
1019 staining (Dcp-1, green) to label apoptotic cells. Nuclei (red) are labeled with TOPRO-3.
1020 Confocal sections show that apoptotic cells in control and mutant tissue were found
1021 outside the neuroepithelial cells. (D) Images of volume-rendering 3D reconstructions of
1022 control and mutant mid L3 OLs with mitotic clones (green) in the OPC and IPC. Anti-
1023 E-cadherin (E-cad, gray) labels neuroepithelial cells. Magenta and blue spheres
1024 represent cells in OPC and IPC clones, respectively. Quantification and comparison of
1025 the number of cells per OPC and IPC clone in the control and mutant background. (E)
1026 Images of volume-rendering 3D reconstructions of segmented mitotic clones in type I
1027 neuroblast in mid L3 control and mutant animals. The clone is labeled in green. Anti-

1028 Dpn staining (Dpn, red) identifies the neuroblast. TOPRO-3 labels the nuclei of cells in
1029 the clone. Quantification and comparison of the number of cells per clone in type I
1030 neuroblast clones in control and mutant animals. (F) Quantification and comparison of
1031 cell death (Dcp-1^{+}/TOPRO-3^{+} puncta) in mid L3 brain hemispheres. (G) Graphic
1032 showing the diameter of larval hemispheres at different L3 stages in control and mutant
1033 animals. Error bars indicate standard deviation. Comparisons between control and
1034 mutant diameters at each larval stage are shown. *p*-values were calculated with the
1035 parametric Turkey's test. The growth rate between larval stages in controls and mutants
1036 is indicated at the top of the graphic. (H, I) Quantifications and comparisons of adult OL
1037 (H) and CB (I) size for *14007/Df* animals and controls. (J, K) Quantifications and
1038 comparisons of adult OL (J) and CB (K) size in cortex glia-specific rescue experiment
1039 brains and the appropriate controls. Control brains represent genotypes for both the
1040 GAL4 driver and the UAS transgene in the mutant background since they could not be
1041 distinguished in the genetic scheme of the experiment (*mir-8*^{glia} control and *UAS-ClC-a*
1042 control). For cortex glia-specific driver details, see Materials and Methods and
1043 Supplementary Figure 7.
1044 OPC, outer proliferation center; IPC, inner proliferation center. Scale bars represent 10
1045 µm. n.s.>0.05, ** p<0.01, *** p<0.001.
1046 (See also Supplementary Figures 6 and 7)
1047
1048 **Figure 5. Strong reduction in a subset of ClC-a^{+} ensheathing glial cells and the**
1049 **neuroblast defects that caused it are observed in *ClC-a* mutants.**
1050 (A-M) Developmental analysis of cells that express *ClC-a* in the OL region in control
1051 animals (*05423*$^{ClC\text{-}a\text{-}GAL4}$ /+) and those same cells in *ClC-a* mutant animals (*05423*$^{ClC\text{-}a\text{-}}$
1052 ^{GAL4} */14007*). Cortex glia membranes are shown in green and nuclei in red. All glial

1053 nuclei were labeled with anti-Repo antibody (blue). (A-D) Images of the ClC-a$^+$ glial
1054 barrier from early to late L3 control OLs with the corresponding schematics, in frontal
1055 views (A-C) and horizontal view (D). (A-C) Volume-rendering 3D reconstructions
1056 showing the ClC-a$^+$ boundary glia population in early (A) and mid (B) L3, and its
1057 division into pag and Xg$_o$ in late L3 (C). (D) Confocal section. The schematic includes
1058 photoreceptors, not labeled in (D) but shown in (F). (E) *ClC-a* expression pattern in the
1059 adult OL. The inner and outer chiasms are correctly formed. (F) Photoreceptor axons
1060 (24B10, gray) in late L3 OLs. For their position relative to glia, see the horizontal view
1061 schematic. (G-J) Images showing which of the glial cells that would normally express
1062 *ClC-a* in control OLs are still present in *ClC-a* mutant OLs from early to late L3 larval
1063 stages, with the corresponding schematics, in frontal views (G-I) and horizontal view
1064 (J). (G-I) Volume-rendering 3D reconstructions. (J) Confocal section. The schematic
1065 shows the aberrant trajectory that some photoreceptor axons can take in (L). (K) *ClC-a*
1066 expression pattern in the mutant adult OL. The inner and outer chiasms are defective.
1067 (L) Photoreceptor axons (24B10, gray) in late L3 mutant OLs. For their position relative
1068 to glia, see the horizontal view schematic. (M) Quantification and comparison of ClC-
1069 a$^+$/Repo$^+$ nuclei in the OL region. *p*-values were calculated with the non-parametric
1070 Mann-Whitney test. (N-U) Analysis of type II DL neuroblast lineages in the CB. (N)
1071 Schematic showing the relative position of DM and DL lineages. (O-Q) Volume-
1072 rendering 3D reconstructions of late L3 control (*14007/+,* O) and mutant (*14007/Df,* P,
1073 Q) brain hemispheres showing type II lineages labeled with the R9D11-tdtomato (red).
1074 Gray and blue spheres mark the position of the DM and DL neuroblasts, respectively.
1075 (R) Confocal image showing the DL1/2 cluster lineages (red), the neuroblast (asterisk),
1076 and mature INPs (arrowheads) labeled with anti-Deadpan (Dpn, blue), and cortex glia
1077 membranes (green) surrounding the neuroblast and encasing the lineage in a glial

1078 chamber. (S, T) Volume-rendering 3D reconstructions of DL1/2 cluster lineages (red)
1079 from control (S) and mutant (T) brains where blue spheres mark the neuroblasts, smaller
1080 yellow spheres mark mature INPs of one of the lineages, and green spheres mark those
1081 from the other lineage. (U) Quantification of the number of INPs per DL lineage,
1082 showing comparisons between the number of INPs in the two lineages (green and
1083 yellow box plots) from controls and mutants. *p*-values were calculated using the non-
1084 parametric Wilcoxon matched-pairs squad rank test. Comparison of number of INPs of
1085 lineages with the highest INPs (green box plots) between control and mutants is shown.
1086 Comparison of number of INPs of lineages with the lowest INPs (yellow box plots)
1087 between control and mutants is shown. In both comparisons, *p*-values were calculated
1088 with the non-parametric Mann-Whitney test.
1089 OPC, outer proliferation center; IPC, inner proliferation center; cxg, cortex glia; bg,
1090 boundary glia; sg, satellite glia; pag, palisade glia; Xg_o, outer chiasm glia; eg, epithelial
1091 glia; mg, marginal glia; me, medulla. Scale bars represent 10 µm. * $p<0.05$ ** $p<0.01$,
1092 *** $p<0.001$.
1093 (See also Supplementary Figures 8 and 9)
1094
1095 **Figure 6. Boundary glia, which express the chemorepellent molecule Slit, are in**
1096 **close contact with photoreceptor axons as they innervate the OL.**
1097 (A-D) Spatiotemporal relationship between photoreceptors and boundary glial cells.
1098 Number of photoreceptor rows was inferred from $24B10^+$ rows in the eye imaginal disc.
1099 (A, B) Horizontal views of mid L3 optic lobe showing ClC-a^+ glia and one (A) and two
1100 (B) rows of R8 photoreceptors (Chaoptin, gray). (C) Same view and staining as panels
1101 A and B of a slightly older brain innervated by six rows of photoreceptors. (D) Frontal
1102 view showing transversal sections between the line of Xg_o cell bodies of photoreceptors

1103 on their way to the medulla. (E, F) Larval (E) and adult (F) examples of photoreceptor
1104 (24B10, gray) phenotypes in *ClC-a* mutants classified as strong. (G, H) Larval (G) and
1105 adult (H) photoreceptor (GMR-GFP, gray) phenotypes in $slit^{dui}$ mutants. Arrowheads
1106 show misguided axons innervating the medulla from its proximal face. (I-K)
1107 Developmental analysis of Slit expression in glial cells in the barrier. Schematics for the
1108 view in each of the stages analyzed are shown. (J) and (K) schematics include
1109 photoreceptors for orientation although they are not labeled in the images. Anti-Repo
1110 (blue) was used to label glial nuclei. A Slit-GFP protein trap (*sli[MI03825-GFSTF.2]*)
1111 that outlines membranes of *slit* expressing cells (Supplementary Figure 10) was used to
1112 visualize the *slit* expression pattern (red, I'-K'). ClC-a^+ boundary glia (green, I"-K") are
1113 outlined (white dashed line) in (I-I",J-J"). Xg_o and palisade glia are outlined in (K-K").
1114 Although *ClC-a* expression is downregulated in (K"), we have shown that they express
1115 *ClC-a* in other panels (Fig 1H, Fig 5D, 5P, Supplementary Figure 6K). (I) Frontal view
1116 of an early L3 OL. (J) Horizontal view of a mid L3 OL. (K) Horizontal view of a late
1117 L3 OL. (L, M) Phenotype analysis for *slit/ClC-a* genetic interaction (M) and *slit*
1118 knockdown (L). Phenotype penetrance and expressivity for each condition is depicted
1119 as the percentage of brains with no phenotype, weak, medium, and strong phenotypes. n
1120 $\geq$ 20 brains for each condition. *p*-values were calculated with the Chi square test.
1121 cxg, cortex glia; bg, boundary glia; Bn, Bolwigs nerve; Lp, lamina plexus; Xg_o, outer
1122 chiasm glia; sg, satellite glia; OPC, outer proliferation center; IPC, inner proliferation
1123 center; eg, epithelial glia; mg, marginal glia; pag, palisade glia; me, medulla. Scale bars
1124 represent 10 µm. * $p<0.05$.
1125 (See also Supplementary Figure 10).
1126

1127 **Figure 7. *ClC-a* expression exclusively in cortex glia rescues the formation of**
1128 **boundary glia and photoreceptor guidance defects.**
1129 (A) Schematics depicting the cortex glia-specific rescue experiment. Frontal views of
1130 mid L3 OLs and the DL1 lineage: control (*14007/+*) showing glial nuclei in blue (Repo)
1131 and *ClC-a* expression in green in the CB in cortex glia surrounding the DL1 neuroblast
1132 and its progeny, and in the OL in cortex glia on the neuroepithelia and boundary glia; a
1133 *ClC-a* mutant (*14007/Df*) showing the absence of *ClC-a* expression and boundary glia;
1134 and an animal where *ClC-a* expression has been exclusively restored in cortex glia
1135 (*mir-8*^{cxg}), resulting in the recovery of boundary cortex glia that do not express *ClC-a*
1136 because they are a subtype of ensheathing glia. (B) Quantification and comparisons of
1137 glial nuclei (Repo, blue) in control, mutant, and rescue animals. *p*-values were
1138 calculated with the non-parametric Mann-Whitney test. (C) Quantification of
1139 photoreceptor guidance phenotypes in control and rescue brains. Control brains
1140 represent genotypes for both the GAL4 driver and the UAS transgene since they could
1141 not be distinguished in the genetic scheme of the experiment (*mir-8*^{glia} control and *UAS-*
1142 *ClC-a* control).
1143 Scale bars represent 10 µm. * $p<0.05$, ** $p<0.01$, *** $p<0.001$.
1144
1145 **Figure 8. Guidance defects in mushroom body neurons.**
1146 (A) Schematic of a mushroom body (MB) in one hemisphere. Dashed lines indicate the
1147 position of imaging planes and associated letters indicate correspondence to panels. The
1148 axonal component of the MB, which consists of the peduncle and lobes, is shown in red,
1149 representing anti-Fasciclin II (FasII) antibody staining. (B-E) Mushroom body analysis
1150 in control brains (late L3 *05423*$^{ClC\text{-}a\text{-}GAL4}$ /+ or mid L3 *14007/+*). (B) Confocal section
1151 though the calyx region of a control brain showing ClC-a^{+} glial membranes (green) and

1152 all nuclei (blue, TOPRO-3). (C) Transversal section through the peduncle of a control
1153 brain. (D) Longitudinal section of the peduncle showing ClC-a^{+} tract-ensheathing glia
1154 surrounding it (arrow). (E) Volume-rendering 3D reconstruction of a control brain
1155 hemisphere showing N-cadherin positive neuropils. (F-I) Mushroom body analysis in
1156 *ClC-a* mutant brains (late L3 *05423*$^{ClC\text{-}a\text{-}GAL4}$ */14007* or mid L3 *14007/Df*) with the same
1157 staining as the equivalent control panels. Compare to panels (F) to (B), (G) to (C), (H)
1158 to (D), and (I) to (E). (J-O) Schematic (J) and volume-rendering 3D reconstructions and
1159 confocal sections of mushroom body neuroblast clones in control (K, L) and *ClC-a*
1160 mutant (M-O) brains labeled in green. (K) Control clone. (L) Cross section of a control
1161 clone at the level of the peduncle. (M) Mutant clone. (N) Cross section at the level of
1162 the peduncle of a mutant clone in M. (O) Mutant clone with a strong phenotype.
1163 Ca, calyx; Pe, peduncle; mL, medial lobe; vL, vertical lobe. Scale bars represent 10 µm.
1164

1165 **REFERENCES**

1166 Apitz H, Salecker I. 2015. A region-specific neurogenesis mode requires migratory
1167 progenitors in the Drosophila visual system. *Nat Neurosci* **18**. doi:10.1038/nn.3896
1168 Apitz H, Salecker I. 2014. A challenge of numbers and diversity: Neurogenesis in the
1169 drosophila optic lobe. *J Neurogenet* **28**:233–249.
1170 doi:10.3109/01677063.2014.922558
1171 Bailey AP, Koster G, Guillermier C, Hirst EMA, MacRae JI, Lechene CP, Postle AD,
1172 Gould AP. 2015. Antioxidant Role for Lipid Droplets in a Stem Cell Niche of
1173 Drosophila. *Cell* **163**:340–353. doi:10.1016/j.cell.2015.09.020
1174 Barres BA. 1991. Glial ion channels. *Curr-Opin-Neurobiol* **1**:354–4388.
1175 doi:10.1016/0959-4388(91)90052-9
1176 Barres B a, Chun LL, Corey DP. 1990. Ion channels in vertebrate glia. *Annu Rev*

1177 *Neurosci* **13**:441–474. doi:10.1146/annurev.neuro.13.1.441
1178 Bazargani N, Attwell D. 2016. Astrocyte calcium signaling: the third wave. *Nat*
1179 *Neurosci* **19**:182.
1180 Bellaïche Y, Gho M, Kaltschmidt JA, Brand AH, Schweisguth F. 2001. Frizzled
1181 regulates localization of cell-fate determinants and mitotic spindle rotation during
1182 asymmetric cell division. *Nat Cell Biol* **3**:50–57. doi:10.1038/35050558
1183 Bellot-Saez A, Kékesi O, Morley JW, Buskila Y. 2017. Astrocytic modulation of
1184 neuronal excitability through K+spatial buffering. *Neurosci Biobehav Rev* **77**:87–
1185 97. doi:10.1016/j.neubiorev.2017.03.002
1186 Bjornsson CS, Apostolopoulou M, Tian Y, Temple S. 2015. It takes a village:
1187 Constructing the neurogenic niche. *Dev Cell* **32**:435–446.
1188 doi:10.1016/j.devcel.2015.01.010
1189 Black JA, Waxman SG. 2013. Noncanonical roles of voltage-gated sodium channels.
1190 *Neuron* **80**:280–291. doi:10.1016/j.neuron.2013.09.012
1191 Blanz J, Schweizer M, Auberson M, Maier H, Muenscher A, Hübner C a, Jentsch TJ.
1192 2007. Leukoencephalopathy upon disruption of the chloride channel ClC-2. *J*
1193 *Neurosci* **27**:6581–9. doi:10.1523/JNEUROSCI.0338-07.2007
1194 Bockenhauer D, Feather S, Stanescu H, Bandulik S, Zdebik A, et al. 2009. Epilepsy,
1195 Ataxia, Sensorineural Deafness, Tubulopathy, and KCNJ10 mutations. *N Engl J*
1196 *Med* **360**:1960–70.
1197 Boone JQ, Doe CQ. 2008. Identification of Drosophila type II neuroblast lineages
1198 containing transit amplifying ganglion mother cells. *Dev Neurobiol* **68**:1185–1195.
1199 doi:10.1002/dneu.20648
1200 Bösl MR, Stein V, Hübner C, Zdebik a a, Jordt SE, Mukhopadhyay a K, Davidoff MS,
1201 Holstein a F, Jentsch TJ. 2001. Male germ cells and photoreceptors, both

1202 dependent on close cell-cell interactions, degenerate upon ClC-2 Cl(-) channel
1203 disruption. *EMBO J* **20**:1289–99. doi:10.1093/emboj/20.6.1289
1204 Cabrero P, Terhzaz S, Romero MF, Davies SA, Blumenthal EM, Dow JAT. 2014.
1205 Chloride channels in stellate cells are essential for uniquely high secretion rates in
1206 neuropeptide-stimulated *Drosophila* diuresis. *Proc Natl Acad Sci* **111**:14301–
1207 14306. doi:10.1073/pnas.1412706111
1208 Carswell KS, Papoutsakis ET. 2000. Extracellular pH affects the proliferation of
1209 cultured human T cells and their expression of the interleukin-2 receptor. *J*
1210 *Immunother* **23**:669–674. doi:10.1097/00002371-200011000-00008
1211 Catalán M, Niemeyer MI, Cid LP, Sepúlveda F V. 2004. Basolateral ClC-2 Chloride
1212 Channels in Surface Colon Epithelium: Regulation by a Direct Effect of
1213 Intracellular Chloride. *Gastroenterology* **126**:1104–1114.
1214 doi:10.1053/j.gastro.2004.01.010
1215 Celniker SE, Dillon LAL, Gerstein MB, Gunsalus KC, Henikoff S, Karpen GH, Kellis
1216 M, Lai EC, Lieb JD, MacAlpine DM, Micklem G, Piano F, Snyder M, Stein L,
1217 White KP, Waterston RH. 2009. Unlocking the secrets of the genome. *Nature*
1218 **459**:927–930. doi:10.1038/459927a
1219 Chell JM, Brand AH. 2010. Nutrition-responsive glia control exit of neural stem cells
1220 from quiescence. *Cell* **143**:1161–1173. doi:10.1016/j.cell.2010.12.007
1221 Chen C, Ouyang W, Grigura V, Zhou Q, Carnes K, Lim H, Zhao GQ, Arber S, Kurpios
1222 N, Murphy TL, Cheng AM, Hassell JA, Chandrashekar V, Hofmann MC, Hess
1223 RA, Murphy KM. 2005. ERM is required for transcriptional control of the
1224 spermatogonial stem cell niche. *Nature* **436**:1030–1034. doi:10.1038/nature03894
1225 Cheng LY, Bailey AP, Leevers SJ, Ragan TJ, Driscoll PC, Gould AP. 2011. Anaplastic
1226 lymphoma kinase spares organ growth during nutrient restriction in drosophila.

1227 *Cell* **146**:435–447. doi:10.1016/j.cell.2011.06.040
1228 Chotard C, Salecker I. 2008. Glial cell development and function in the Drosophila
1229 visual system. *Neuron Glia Biol* **3**:17–25. doi:10.1017/S1740925X07000592.Glial
1230 Chotard C, Salecker I. 2004. Neurons and glia: Team players in axon guidance. *Trends*
1231 *Neurosci* **27**:655–661. doi:10.1016/j.tins.2004.09.001
1232 Ciapa B, Philippe L. 2013. Intracellular and Extracellular pH and Ca Are Bound to
1233 Control Mitosis in the Early Sea Urchin Embryo via ERK and MPF Activities.
1234 *PLoS One* **8**. doi:10.1371/journal.pone.0066113
1235 Corty MM, Freeman MR. 2013. Architects in neural circuit design: Glia control neuron
1236 numbers and connectivity. *J Cell Biol* **203**:395–405. doi:10.1083/jcb.201306099
1237 Coutinho-Budd JC, Sheehan AE, Freeman MR. 2017. The secreted neurotrophin spätzle
1238 3 promotes glial morphogenesis and supports neuronal survival and function.
1239 *Genes Dev* **31**:2023–2038. doi:10.1101/gad.305888.117
1240 Dearborn R. 2004. An axon scaffold induced by retinal axons directs glia to destinations
1241 in the Drosophila optic lobe. *Development* **131**:2291–2303. doi:10.1242/dev.01111
1242 Denholm B, Hu N, Fauquier T, Caubit X, Fasano L, Skaer H. 2013. The tiptop/teashirt
1243 genes regulate cell differentiation and renal physiology in Drosophila.
1244 *Development* **140**:1100–1110. doi:10.1242/dev.088989
1245 Depienne C, Bugiani M, Dupuits C, Galanaud D, Touitou V, Postma N, van Berkel C,
1246 Polder E, Tollard E, Darios F, Brice A, de Die-Smulders CE, Vles JS, Vanderver
1247 A, Uziel G, Yalcinkaya C, Frints SG, Kalscheuer VM, Klooster J, Kamermans M,
1248 Abbink TEM, Wolf NI, Sedel F, van der Knaap MS. 2013. Brain white matter
1249 oedema due to ClC-2 chloride channel deficiency: An observational analytical
1250 study. *Lancet Neurol* **12**:659–668. doi:10.1016/S1474-4422(13)70053-X
1251 Diao F, Ironfield H, Luan H, Diao F, Shropshire WC, Ewer J, Marr E, Potter CJ,

1252 Landgraf M, White BH. 2015. Plug-and-play genetic access to drosophila cell
1253 types using exchangeable exon cassettes. *Cell Rep* **10**:1410–1421.
1254 doi:10.1016/j.celrep.2015.01.059
1255 Doe CQ. 2008. Neural stem cells: balancing self-renewal with differentiation.
1256 *Development* **135**:1575–1587. doi:10.1242/dev.014977
1257 Dumstrei K, Wang F, Hartenstein V. 2003. Role of DE-cadherin in neuroblast
1258 proliferation, neural morphogenesis, and axon tract formation in *Drosophila* larval
1259 brain development. *J Neurosci* **23**:3325–3335.
1260 Edwards MM, Marín de Evsikova C, Collin GB, Gifford E, Wu J, Hicks WL, Whiting
1261 C, Varvel NH, Maphis N, Lamb BT, Naggert JK, Nishina PM, Peachey NS. 2010.
1262 Photoreceptor degeneration, azoospermia, leukoencephalopathy, and abnormal
1263 RPE cell function in mice expressing an early stop mutation in CLCN2. *Invest*
1264 *Ophthalmol Vis Sci* **51**:3264–72. doi:10.1167/iovs.09-4887
1265 Egger B, Gold KS, Brand AH. 2010. Notch regulates the switch from symmetric to
1266 asymmetric neural stem cell division in the Drosophila optic lobe. *Development*
1267 **137**:2981–2987. doi:10.1242/dev.051250
1268 Evans CJ, Olson JM, Ngo KT, Kim E, Lee NE, Kuoy E, Patananan AN, Sitz D, Tran
1269 PT, Do MT, Yackle K, Cespedes A, Hartenstein V, Call GB, Banerjee U. 2009. G-
1270 TRACE: Rapid Gal4-based cell lineage analysis in Drosophila. *Nat Methods*
1271 **6**:603–605. doi:10.1038/nmeth.1356
1272 Fan Y, Soller M, Flister S, Hollmann M, Müller M, Bello B, Egger B, White K, Schäfer
1273 MA, Reichert H. 2005. The egghead gene is required for compartmentalization in
1274 Drosophila optic lobe development. *Dev Biol* **287**:61–73.
1275 doi:10.1016/j.ydbio.2005.08.031
1276 Fernandes-Rosa FL, Daniil G, Orozco IJ, Göppner C, El Zein R, Jain V, Boulkroun S,

1277 Jeunemaitre X, Amar L, Lefebvre H, Schwarzmayr T, Strom TM, Jentsch TJ,
1278 Zennaro MC. 2018. A gain-of-function mutation in the CLCN2 chloride channel
1279 gene causes primary aldosteronism. *Nat Genet* **50**:355–361. doi:10.1038/s41588-
1280 018-0053-8
1281 Fietz SA, Kelava I, Vogt J, Wilsch-Bräuninger M, Stenzel D, Fish JL, Corbeil D, Riehn
1282 A, Distler W, Nitsch R, Huttner WB. 2010. OSVZ progenitors of human and ferret
1283 neocortex are epithelial-like and expand by integrin signaling. *Nat Neurosci*
1284 **13**:690–699. doi:10.1038/nn.2553
1285 Flinck M, Kramer SH, Pedersen SF. 2018. Roles of pH in control of cell proliferation.
1286 *Acta Physiol* **223**:1–17. doi:10.1111/apha.13068
1287 Flores CA, Niemeyer MI, Sepúlveda F V, Cid LP. 2009. Two splice variants derived
1288 from a Drosophila melanogaster candidate ClC gene generate ClC-2-type Cl-
1289 channels. *Mol Membr Biol* **23**:149–56. doi:10.1080/09687860500449978
1290 Földy C, Lee SH, Morgan RJ, Soltesz I. 2010. Regulation of fast-spiking basket cell
1291 synapses by the chloride channel ClC-2. *Nat Neurosci* **13**:1047–1049.
1292 doi:10.1038/nn.2609
1293 Freeman MR, Doherty J. 2006. Glial cell biology in Drosophila and vertebrates. *Trends*
1294 *Neurosci* **29**:82–90. doi:10.1016/j.tins.2005.12.002
1295 González F, Romani S, Cubas P, Modolell J, Campuzano S. 1989. Molecular analysis
1296 of the asense gene, a member of the achaete-scute complex of Drosophila
1297 melanogaster, and its novel role in optic lobe development. *EMBO J* **8**:3553–3562.
1298 doi:10.1002/J.1460-2075.1989.TB08527.X
1299 Han C, Jan LY, Jan Y-N. 2011. Enhancer-driven membrane markers for analysis of
1300 nonautonomous mechanisms reveal neuron-glia interactions in Drosophila. *Proc*
1301 *Natl Acad Sci* **108**:9673–9678. doi:10.1073/pnas.1106386108

1302 Hansen D V., Lui JH, Parker PRL, Kriegstein AR. 2010. Neurogenic radial glia in the
1303 outer subventricular zone of human neocortex. *Nature* **464**:554–561.
1304 doi:10.1038/nature08845
1305 Hoegg-Beiler MB, Sirisi S, Orozco IJ, Ferrer I, Hohensee S, Auberson M, Gödde K,
1306 Vilches C, De Heredia ML, Nunes V, Estévez R, Jentsch TJ. 2014. Disrupting
1307 MLC1 and GlialCAM and ClC-2 interactions in leukodystrophy entails glial
1308 chloride channel dysfunction. *Nat Commun* **5**. doi:10.1038/ncomms4475
1309 Hofbauer A, Campos-Ortega J. 1990. Proliferation and and early differentiation of the
1310 optic lobes in Drosophila melanogaster. *Roux's Arch Dev Biol* 264–274.
1311 Hou X, Zhang R, Wang J, Li Y, Li F, Zhang Y, Zheng X, Shen Y, Wang Y, Zhou L.
1312 2018. CLC-2 is a positive modulator of oligodendrocyte precursor cell
1313 differentiation and myelination. *Mol Med Rep* **17**:4515–4523.
1314 doi:10.3892/mmr.2018.8439
1315 Hoyle G, Williams M, Phillips C. 1986. Functional morphology of insect neuronal cell-
1316 surface/glial contacts: The trophospongium. *J Comp Neurol* **256**:113–28.
1317 Jentsch TJ, Pusch M. 2018. CLC Chloride Channels and Transporters: Structure,
1318 Function, Physiology, and Disease. *Physiol Rev* **98**:1493–1590.
1319 doi:10.1152/physrev.00047.2017
1320 Jeworutzki E, López-Hernández T, Capdevila-Nortes X, Sirisi S, Bengtsson L,
1321 Montolio M, Zifarelli G, Arnedo T, Müller CS, Schulte U, Nunes V, Martínez A,
1322 Jentsch TJ, Gasull X, Pusch M, Estévez R. 2012. GlialCAM, a protein defective in
1323 a leukodystrophy, serves as a ClC-2 Cl(-) channel auxiliary subunit. *Neuron*
1324 **73**:951–61. doi:10.1016/j.neuron.2011.12.039
1325 Jordt SE, Jentsch TJ. 1997. Molecular dissection of gating in the CIC-2 chloride
1326 channel. *EMBO J* **16**:1582–1592. doi:10.1093/emboj/16.7.1582

1327 Kahanovitch U, Cuddapah VA, Pacheco NL, Holt LM, Mulkey DK, Percy AK, Olsen
1328 ML. 2018. MeCP2 Deficiency Leads to Loss of Glial Kir4.1. *Eneuro*
1329 **2**:ENEURO.0194-17.2018. doi:10.3923/JBS.2017.394.399
1330 Kanai MI, Kim MJ, Akiyama T, Takemura M, Wharton K, O'Connor MB, Nakato H.
1331 2018. Regulation of neuroblast proliferation by surface glia in the Drosophila
1332 larval brain. *Sci Rep* **8**:1–15. doi:10.1038/s41598-018-22028-y
1333 Karres JS, Hilgers V, Carrera I, Treisman J, Cohen SM. 2007. The Conserved
1334 microRNA MiR-8 Tunes Atrophin Levels to Prevent Neurodegeneration in
1335 Drosophila. *Cell* **131**:136–145. doi:10.1016/j.cell.2007.09.020
1336 Kearney JB, Wheeler SR, Estes P, Parente B, Crews ST. 2004. Gene expression
1337 profiling of the developing Drosophila CNS midline cells. *Dev Biol* **275**:473–492.
1338 doi:10.1016/j.ydbio.2004.08.047
1339 Khakh BS, McCarthy KD. 2015. Astrocyte calcium signaling: From observations to
1340 functions and the challenges therein. *Cold Spring Harb Perspect Biol* **7**:1–18.
1341 doi:10.1101/cshperspect.a020404
1342 Kremer MC, Jung C, Batelli S, Rubin GM, Gaul U. 2017. The glia of the adult
1343 Drosophila nervous system. *Glia* **65**:606–638. doi:10.1002/glia.23115
1344 Lee BP, Jones BW. 2005. Transcriptional regulation of the Drosophila glial gene repo.
1345 *Mech Dev* **122**:849–862. doi:10.1016/j.mod.2005.01.002
1346 Li G-R. 2011. Functional ion channels in stem cells. *World J Stem Cells* **3**:19.
1347 doi:10.4252/wjsc.v3.i3.19
1348 Liebau S, Kleger A, Levin M, Yu SP. 2013. Stem cells and ion channels. *Stem Cells Int*
1349 **2013**. doi:10.1155/2013/238635
1350 Lioy DT, Garg SK, Monaghan CE, Raber J, Foust KD, Kaspar BK, Hirrlinger PG,
1351 Kirchhoff F, Bissonnette JM, Ballas N, Mandel G. 2011. A role for glia in the

1352 progression of Rett-syndrome. *Nature* **475**:497–500. doi:10.1038/nature10214
1353 Makara JK, Rappert A, Matthias K, Steinhäuser C, Spät A, Kettenmann H. 2003.
1354 Astrocytes from mouse brain slices express ClC-2-mediated Cl-currents regulated
1355 during development and after injury. *Mol Cell Neurosci* **23**:521–530.
1356 doi:10.1016/S1044-7431(03)00080-0
1357 Mayer B, Emery G, Berdnik D, Wirtz-Peitz F, Knoblich JA. 2005. Quantitative analysis
1358 of protein dynamics during asymmetric cell division. *Curr Biol* **15**:1847–1854.
1359 doi:10.1016/j.cub.2005.08.067
1360 Morante J, Vallejo DM, Desplan C, Dominguez M. 2013. Conserved miR-8/miR-200
1361 defines a glial niche that controls neuroepithelial expansion and neuroblast
1362 transition. *Dev Cell* **27**:174–187. doi:10.1016/j.devcel.2013.09.018
1363 Moroni RF, Inverardi F, Regondi MC, Pennacchio P, Frassoni C. 2015. Developmental
1364 expression of Kir4.1 in astrocytes and oligodendrocytes of rat somatosensory
1365 cortex and hippocampus. *Int J Dev Neurosci* **47**:198–205.
1366 doi:10.1016/j.ijdevneu.2015.09.004
1367 Nagarkar-Jaiswal S, Deluca SZ, Lee PT, Lin WW, Pan H, Zuo Z, Lv J, Spradling AC,
1368 Bellen HJ. 2015a. A genetic toolkit for tagging intronic MiMIC containing genes.
1369 *Elife* **4**:2–9. doi:10.7554/eLife.08469
1370 Nagarkar-Jaiswal S, Lee P-T, Campbell ME, Chen K, Anguiano-Zarate S, Cantu
1371 Gutierrez M, Busby T, Lin W-W, He Y, Schulze KL, Booth BW, Evans-Holm M,
1372 Venken KJ, Levis RW, Spradling AC, Hoskins R a, Bellen HJ. 2015b. A library of
1373 MiMICs allows tagging of genes and reversible, spatial and temporal knockdown
1374 of proteins in Drosophila. *Elife* **4**:1–28. doi:10.7554/eLife.05338
1375 Nassif C, Noveen A, Hartenstein V. 2003. Early development of the Drosophila brain:
1376 III. The pattern of neuropile founder tracts during the larval period. *J Comp Neurol*

1377 **455**:417–434. doi:10.1002/cne.10482

1378 Ngo KT, Wang J, Junker M, Kriz S, Vo G, Asem B, Olson JM, Banerjee U, Hartenstein
1379 V. 2010. Concomitant requirement for Notch and Jak/Stat signaling during neuro-
1380 epithelial differentiation in the Drosophila optic lobe. *Dev Biol* **346**:284–295.
1381 doi:10.1016/j.ydbio.2010.07.036

1382 Nwaobi SE, Cuddapah VA, Patterson KC, Randolph AC, Olsen ML. 2016. The role of
1383 glial-specific Kir4.1 in normal and pathological states of the CNS. *Acta*
1384 *Neuropathol* **132**:1–21. doi:10.1007/s00401-016-1553-1

1385 Oatley MJ, Racicot KE, Oatley JM. 2011. Sertoli Cells Dictate Spermatogonial Stem
1386 Cell Niches in the Mouse Testis. *Biol Reprod* **84**:639–645.
1387 doi:10.1095/biolreprod.110.087320

1388 Olsen ML, Khakh BS, Skatchkov SN, Zhou M, Lee CJ, Rouach N. 2015. New Insights
1389 on Astrocyte Ion Channels: Critical for Homeostasis and Neuron-Glia Signaling. *J*
1390 *Neurosci* **35**:13827–13835. doi:10.1523/JNEUROSCI.2603-15.2015

1391 Orihara-Ono M, Toriya M, Nakao K, Okano H. 2011. Downregulation of Notch
1392 mediates the seamless transition of individual Drosophila neuroepithelial
1393 progenitors into optic medullar neuroblasts during prolonged G1. *Dev Biol*
1394 **351**:163–175. doi:10.1016/j.ydbio.2010.12.044

1395 Pappalardo L, BLack J, Waxman SG. 2016. Sodium channels in astroglia and
1396 microglia. *Glia* **64**:1628–1645.

1397 Pappu KS, Morey M, Nern A, Spitzweck B, Dickson BJ, Zipursky SL. 2011. Robo-3--
1398 mediated repulsive interactions guide R8 axons during Drosophila visual system
1399 development. *Proc Natl Acad Sci U S A* **108**:7571–7576.

1400 Pereanu W, Shy D, Hartenstein V. 2005. Morphogenesis and proliferation of the larval
1401 brain glia in Drosophila. *Dev Biol* **283**:191–203. doi:10.1016/j.ydbio.2005.04.024

1402 Perez-Gomez R, Slovakova J, Rives-Quinto N, Krejci A, Carmena A. 2013. A Serrate-
1403 Notch-Canoe complex mediates essential interactions between glia and
1404 neuroepithelial cells during Drosophila optic lobe development. *J Cell Sci*
1405 **126**:4873–4884. doi:10.1242/jcs.125617
1406 Perez SE, Steller H. 1996. Migration of glial cells into retinal axon target field in
1407 Drosophila melanogaster. *J Neurobiol* **30**:359–373.
1408 Persi E, Duran-Frigola M, Damaghi M, Roush W, Aloy P, Cleveland J, Gillies R,
1409 Ruppin E. 2018. Systems analysis of intracellular pH vulnerabilities for cancer
1410 therapy. *Nat Commun* **9**:2997.
1411 Plazaola-Sasieta H, Fernández-Pineda A, Zhu Q, Morey M. 2017. Untangling the
1412 wiring of the Drosophila visual system: developmental principles and molecular
1413 strategies. *J Neurogenet* **31**. doi:10.1080/01677063.2017.1391249
1414 Poeck B, Fischer S, Gunning D, Zipursky SL, Salecker I. 2001. Glial cells mediate
1415 target layer selection of retinal axons in the developing visual system of
1416 Drosophila. *Neuron* **29**:99–113. doi:10.1016/S0896-6273(01)00183-0
1417 Ratte S, Prescott SA. 2011. ClC-2 Channels Regulate Neuronal Excitability, Not
1418 Intracellular Chloride Levels. *J Neurosci* **31**:15838–15843.
1419 doi:10.1523/JNEUROSCI.2748-11.2011
1420 Read RD. 2018. Pvr receptor tyrosine kinase signaling promotes post-embryonic
1421 morphogenesis and survival of glia and neural progenitor cells in *Drosophila*.
1422 *Development* dev.164285. doi:10.1242/dev.164285
1423 Reddy BVVG, Rauskolb C, Irvine KD. 2010. Influence of Fat-Hippo and Notch
1424 signaling on the proliferation and differentiation of Drosophila optic
1425 neuroepithelia. *Development* **137**:2397–2408. doi:10.1242/dev.050013
1426 Reillo I, De Juan Romero C, García-Cabezas MÁ, Borrell V. 2011. A Role for

1427 intermediate radial glia in the tangential expansion of the mammalian cerebral
1428 cortex. *Cereb Cortex* **21**:1674–1694. doi:10.1093/cercor/bhq238
1429 Ren Q, Awasaki T, Wang Y-C, Huang Y-F, Lee T. 2018. Lineage-guided Notch-
1430 dependent gliogenesis by *Drosophila* multi-potent progenitors. *Development*
1431 **145**:dev160127. doi:10.1242/dev.160127
1432 Rinke I, Artmann J, Stein V. 2010. ClC-2 Voltage-Gated Channels Constitute Part of
1433 the Background Conductance and Assist Chloride Extrusion. *J Neurosci* **30**:4776–
1434 4786. doi:10.1523/JNEUROSCI.6299-09.2010
1435 Rose U, Derst C, Wanischeck M, Marinc C, Walther C. 2007. Properties and possible
1436 function of a hyperpolarisation-activated chloride current in Drosophila. *J Exp Biol*
1437 **210**:2489–2500. doi:10.1242/jeb.006361
1438 Ruddy RM, Morshead CM. 2018. Home sweet home: the neural stem cell niche
1439 throughout development and after injury. *Cell Tissue Res* **371**:125–141.
1440 doi:10.1007/s00441-017-2658-0
1441 Scholl UI, Choi M, Liu T, Ramaekers VT, Hausler MG, Grimmer J, Tobe SW, Farhi A,
1442 Nelson-Williams C, Lifton RP. 2009. Seizures, sensorineural deafness, ataxia,
1443 mental retardation, and electrolyte imbalance (SeSAME syndrome) caused by
1444 mutations in KCNJ10. *Proc Natl Acad Sci* **106**:5842–5847.
1445 doi:10.1073/pnas.0901749106
1446 Scholl UI, Stölting G, Schewe J, Thiel A, Tan H, Nelson-Williams C, Vichot AA, Jin
1447 SC, Loring E, Untiet V, Yoo T, Choi J, Xu S, Wu A, Kirchner M, Mertins P,
1448 Rump LC, Onder AM, Gamble C, McKenney D, Lash RW, Jones DP, Chune G,
1449 Gagliardi P, Choi M, Gordon R, Stowasser M, Fahlke C, Lifton RP. 2018. CLCN2
1450 chloride channel mutations in familial hyperaldosteronism type II. *Nat Genet*
1451 **50**:349–354. doi:10.1038/s41588-018-0048-5

1452 Shigetomi E, Patel S, Khakh BS. 2016. Probing the Complexities of Astrocyte Calcium
1453 Signaling. *Trends Cell Biol* **26**:300–312. doi:10.1016/j.tcb.2016.01.003
1454 Sicca F, Ambrosini E, Marchese M, Sforna L, Servettini I, Valvo G, Brignone MS,
1455 Lanciotti A, Moro F, Grottesi A, Catacuzzeno L, Baldini S, Hasan S, D'adamo
1456 MC, Franciolini F, Molinari P, Santorelli FM, Pessia M. 2016. Gain-of-function
1457 defects of astrocytic Kir4.1 channels in children with autism spectrum disorders
1458 and epilepsy. *Sci Rep* **6**:1–15. doi:10.1038/srep34325
1459 Sicca F, Imbrici P, D'Adamo MC, Moro F, Bonatti F, Brovedani P, Grottesi A, Guerrini
1460 R, Masi G, Santorelli FM, Pessia M. 2011. Autism with Seizures and Intellectual
1461 Disability: Possible Causative Role of Gain-of-function of the Inwardly-Rectifying
1462 K+Channel Kir4.1. *Neurobiol Dis* **43**:239–247. doi:10.1016/j.nbd.2011.03.016
1463 Sirisi S, Elorza-Vidal X, Arnedo T, Armand-Ugón M, Callejo G, Capdevila-Nortes X,
1464 López-Hernández T, Schulte U, Barrallo-Gimeno A, Nunes V, Gasull X, Estévez
1465 R. 2017. Depolarization causes the formation of a ternary complex between
1466 GlialCAM, MLC1 and ClC-2 in astrocytes: implications in megalencephalic
1467 leukoencephalopathy. *Hum Mol Genet* **26**:2436–2450. doi:10.1093/hmg/ddx134
1468 Smith RS, Kenny CJ, Ganesh V, Jang A, Borges-Monroy R, Partlow JN, Hill RS, Shin
1469 T, Chen AY, Doan RN, Anttonen A-K, Ignatius J, Medne L, Bönnemann CG,
1470 Hecht JL, Salonen O, Barkovich AJ, Poduri A, Wilke M, de Wit MCY, Mancini
1471 GMS, Sztriha L, Im K, Amrom D, Andermann E, Paetau R, Lehesjoki A-E, Walsh
1472 CA, Lehtinen MK. 2018. Sodium Channel SCN3A (NaV1.3) Regulation of Human
1473 Cerebral Cortical Folding and Oral Motor Development. *Neuron* **99**:905–913.e7.
1474 doi:10.1016/j.neuron.2018.07.052
1475 Sousa-Nunes R, Yee LL, Gould AP. 2011. Fat cells reactivate quiescent neuroblasts via
1476 TOR and glial insulin relays in Drosophila. *Nature* **471**:508–513.

1477 doi:10.1038/nature09867
1478 Spéder P, Brand AH. 2018. Systemic and local cues drive neural stem cell niche
1479 remodelling during neurogenesis in drosophila. *Elife* **7**:1–16.
1480 doi:10.7554/eLife.30413
1481 Spéder P, Brand AH. 2014. Gap junction proteins in the blood-brain barrier control
1482 nutrient-dependent reactivation of Drosophila neural stem cells. *Dev Cell* **30**:309–
1483 321. doi:10.1016/j.devcel.2014.05.021
1484 Spindler SR, Ortiz I, Fung S, Takashima S, Hartenstein V. 2009. Drosophila cortex and
1485 neuropile glia influence secondary axon tract growth, pathfinding, and
1486 fasciculation in the developing larval brain. *Dev Biol* **334**:355–368.
1487 doi:10.1016/j.ydbio.2009.07.035
1488 Stork T, Sheehan A, Tasdemir-Yilmaz OE, Freeman MR. 2014. Neuron-Glia
1489 interactions through the heartless fgf receptor signaling pathway mediate
1490 morphogenesis of drosophila astrocytes. *Neuron* **83**:388–403.
1491 doi:10.1016/j.neuron.2014.06.026
1492 Suzuki T, Hasegawa E, Nakai Y, Kaido M, Takayama R, Sato M. 2016. Formation of
1493 Neuronal Circuits by Interactions between Neuronal Populations Derived from
1494 Different Origins in the Drosophila Visual Center. *Cell Rep* **15**:499–509.
1495 doi:10.1016/j.celrep.2016.03.056
1496 Tayler T, Robixaux M, Garrity P. 2004. Compartmentalization of visual centers in the
1497 Drosophila brain requires Slit and Robo proteins. *Development* **131**:5935–5945.
1498 doi:10.1242/dev.01465
1499 Tomancak P, Beaton A, Weiszmann R, Kwan E, Shu S, Lewis SE, Richards S,
1500 Ashburner M, Hartenstein V, Celniker SE, Rubin GM. 2002. Systematic
1501 determination of patterns of gene expression during Drosophila embryogenesis.

1502 *Genome Biol* **3**:RESEARCH0088.

1503 Tomancak P, Berman BP, Beaton A, Weiszmann R, Kwan E, Hartenstein V, Celniker
1504 SE, Rubin GM. 2007. Global analysis of patterns of gene expression during
1505 Drosophila embryogenesis. *Genome Biol* **8**:1–24. doi:10.1186/gb-2007-8-7-r145

1506 Ugarte G, Delgado R, O'Day PM, Farjah F, Cid LP, Vergara C, Bacigalupo J. 2005.
1507 Putative ClC-2 chloride channel mediates inward rectification in Drosophila retinal
1508 photoreceptors. *J Membr Biol* **207**:151–160. doi:10.1007/s00232-005-0810-3

1509 Venken KJT, Schulze KL, Haelterman NA, Pan H, He Y, Evans-Holm M, Carlson JW,
1510 Levis RW, Spradling AC, Hoskins RA, Bellen HJ. 2011. MiMIC: a highly
1511 versatile transposon insertion resource for engineering Drosophila melanogaster
1512 genes. *Nat Methods* **8**:737–743.

1513 Verkhrastsky A, Steinhauser C. 2000. Ion channels in glial cells. *Brain Res* **32**:380–412.

1514 Viktorin G, Riebli N, Reichert H. 2013. A multipotent transit-amplifying neuroblast
1515 lineage in the central brain gives rise to optic lobe glial cells in Drosophila. *Dev*
1516 *Biol* **379**:182–194. doi:10.1016/j.ydbio.2013.04.020

1517 Wang JW, Beck ES, McCabe BD. 2012. A modular toolset for recombination
1518 transgenesis and neurogenetic analysis of Drosophila. *PLoS One* **7**.
1519 doi:10.1371/journal.pone.0042102

1520 Wang W, Li Y, Zhou L, Yue H, Luo H. 2011a. Role of JAK/STAT signaling in
1521 neuroepithelial stem cell maintenance and proliferation in the Drosophila optic
1522 lobe. *Biochem Biophys Res Commun* **410**:714–720.
1523 doi:10.1016/j.bbrc.2011.05.119

1524 Wang W, Liu W, Wang Y, Zhou L, Tang X, Luo H. 2011b. Notch signaling regulates
1525 neuroepithelial stem cell maintenance and neuroblast formation in Drosophila optic
1526 lobe development. *Dev Biol* **350**:414–428.

1527 Weng M, Haenfler JM, Lee CY. 2012. Changes in Notch signaling coordinates
1528 maintenance and differentiation of the Drosophila larval optic lobe neuroepithelia.
1529 *Dev Neurobiol* **72**:1376–1390. doi:10.1002/dneu.20995
1530 White KA, Grillo-Hill BK, Barber DL. 2017. Cancer cell behaviors mediated by
1531 dysregulated pH dynamics at a glance. *J Cell Sci* **130**:663–669.
1532 doi:10.1242/jcs.195297
1533 Yasugi T, Sugie A, Umetsu D, Tabata T. 2010. Coordinated sequential action of EGFR
1534 and Notch signaling pathways regulates proneural wave progression in the
1535 Drosophila optic lobe. *Development* **137**:3193–3203. doi:10.1242/dev.048058
1536 Yasugi T, Umetsu D, Murakami S, Sato M, Tabata T. 2008. Drosophila optic lobe
1537 neuroblasts triggered by a wave of proneural gene expression that is negatively
1538 regulated by JAK/STAT. *Development* **135**:1471–1480. doi:10.1242/dev.019117
1539 Zhu CC, Boone JQ, Jensen PA, Hanna S, Podemski L, Locke J, Doe CQ, O'Connor
1540 MB. 2008. Drosophila Activin- and the Activin-like product Dawdle function
1541 redundantly to regulate proliferation in the larval brain. *Development* **135**:513–521.
1542 doi:10.1242/dev.010876
1543
1544
1545
1546
1547
1548
1549
1550
1551

Figure 1

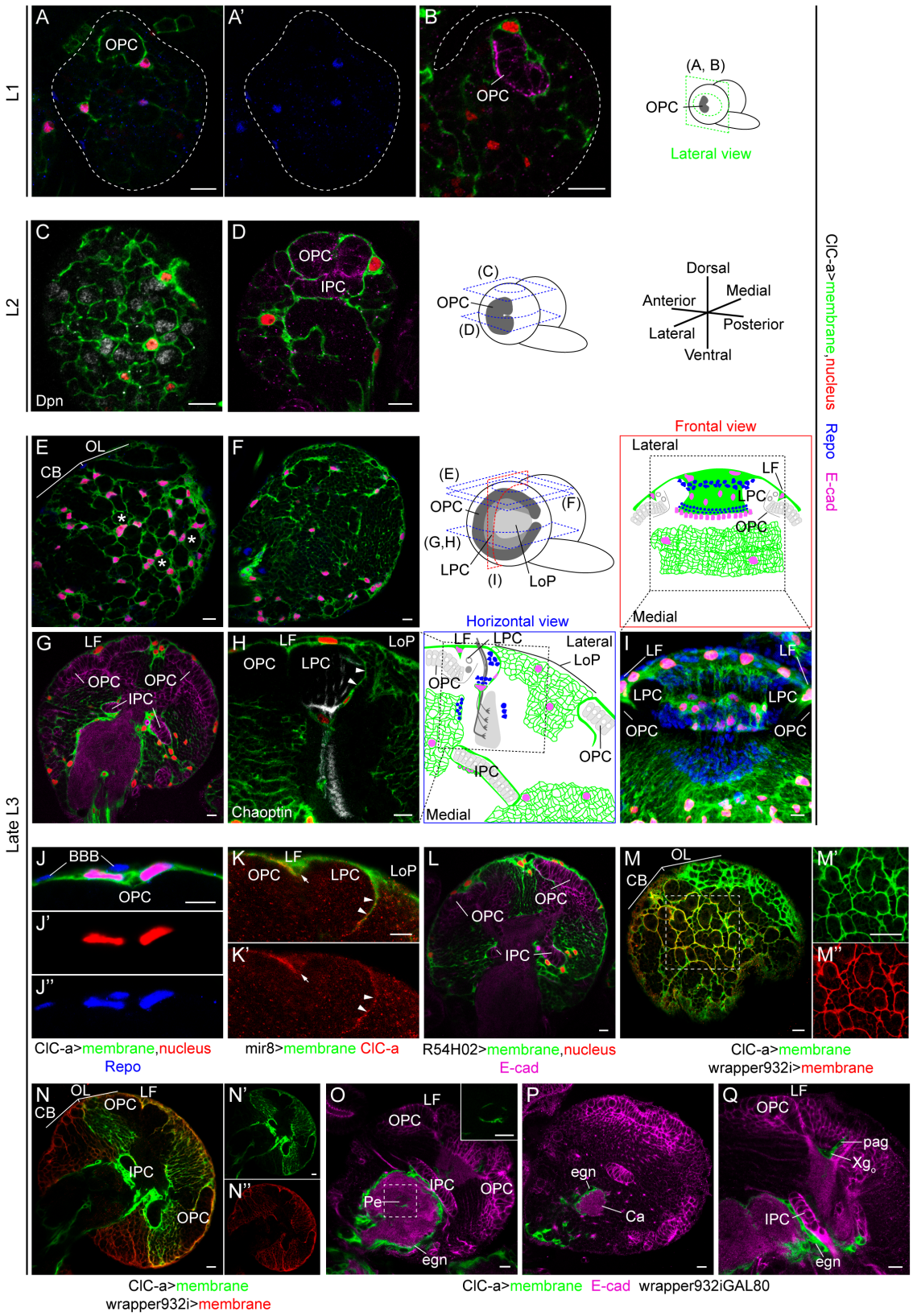
L1
L2
Late L3
A
A'
B
OPC
(A, B)
Lateral view
C
D
Dpn
IPC
(C)
(D)
Dorsal
Medial
Anterior
Posterior
Lateral
Ventral
E
F
OL
CB
(E)
(F)
(G,H)
(I)
LPC
LoP
Frontal view
Lateral
Medial
G
H
LF
Chaoptin
Horizontal view
I
J
BBB
J'
J''
K
K'
L
M
M'
M''
ClC-a>membrane,nucleus
Repo
mir8>membrane ClC-a
R54H02>membrane,nucleus
E-cad
ClC-a>membrane
wrapper932i>membrane
N
N'
N''
O
P
Q
Pe
egn
Ca
pag
Xg
ClC-a>membrane
wrapper932i>membrane
ClC-a>membrane E-cad wrapper932iGAL80
ClC-a>membrane,nucleus Repo E-cad

1555 **Figure 2**

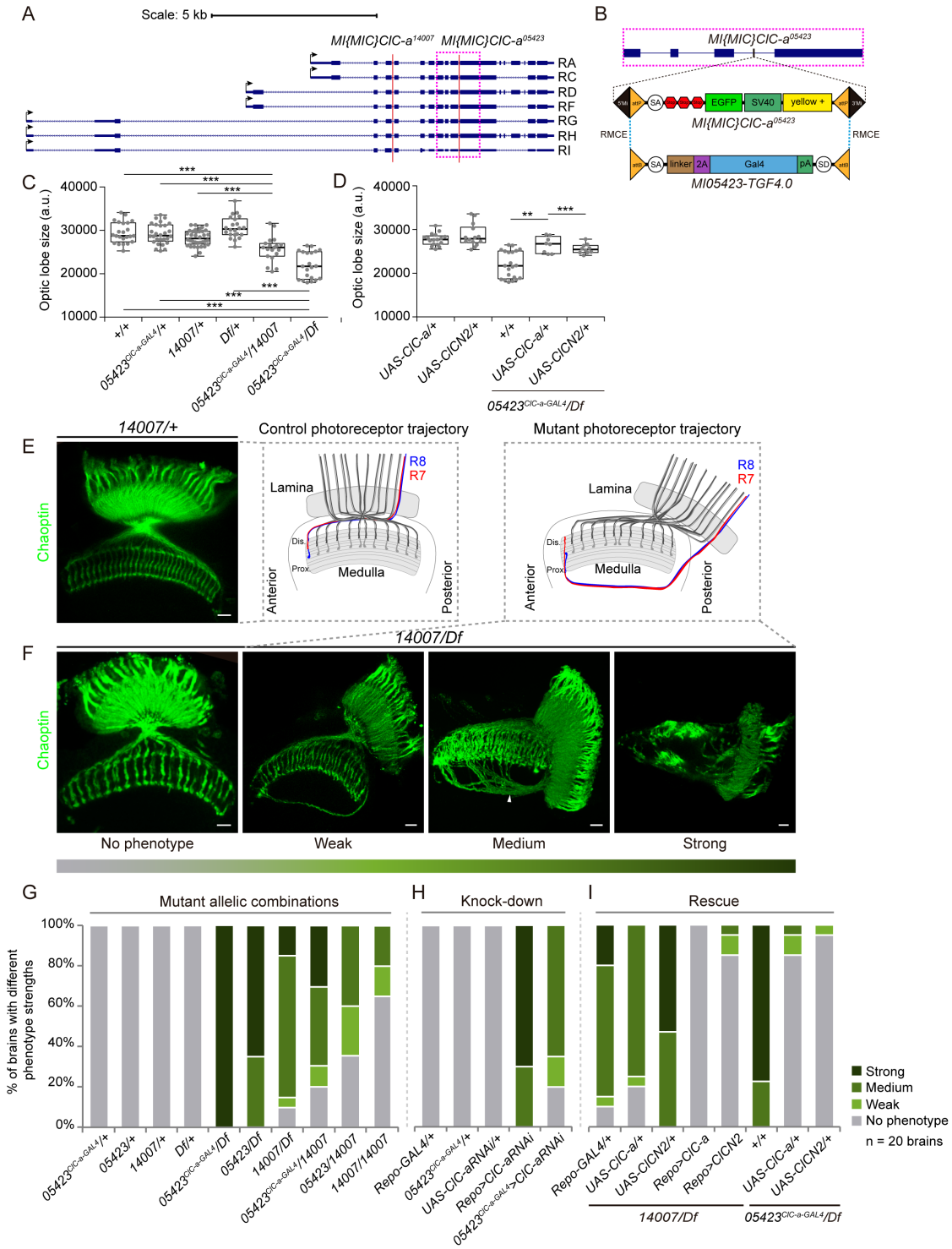

1556

1557

1558

1559

1560

1561 **Figure 3**

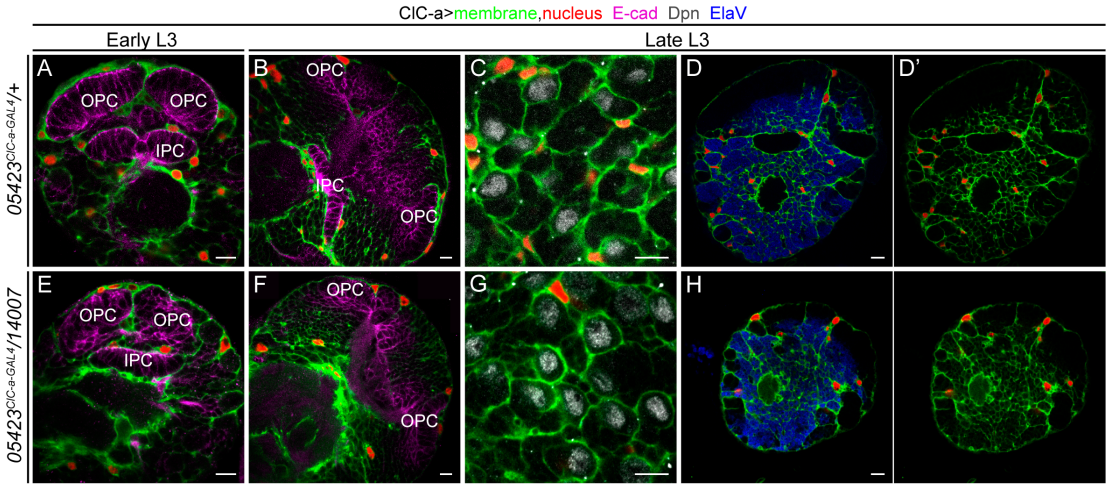

1562

1563

1564

1565

1566

1567

1568

1569

1570

1571

1572

1573

1574

1575

1576

1577

1578

1579

1580 **Figure 4**

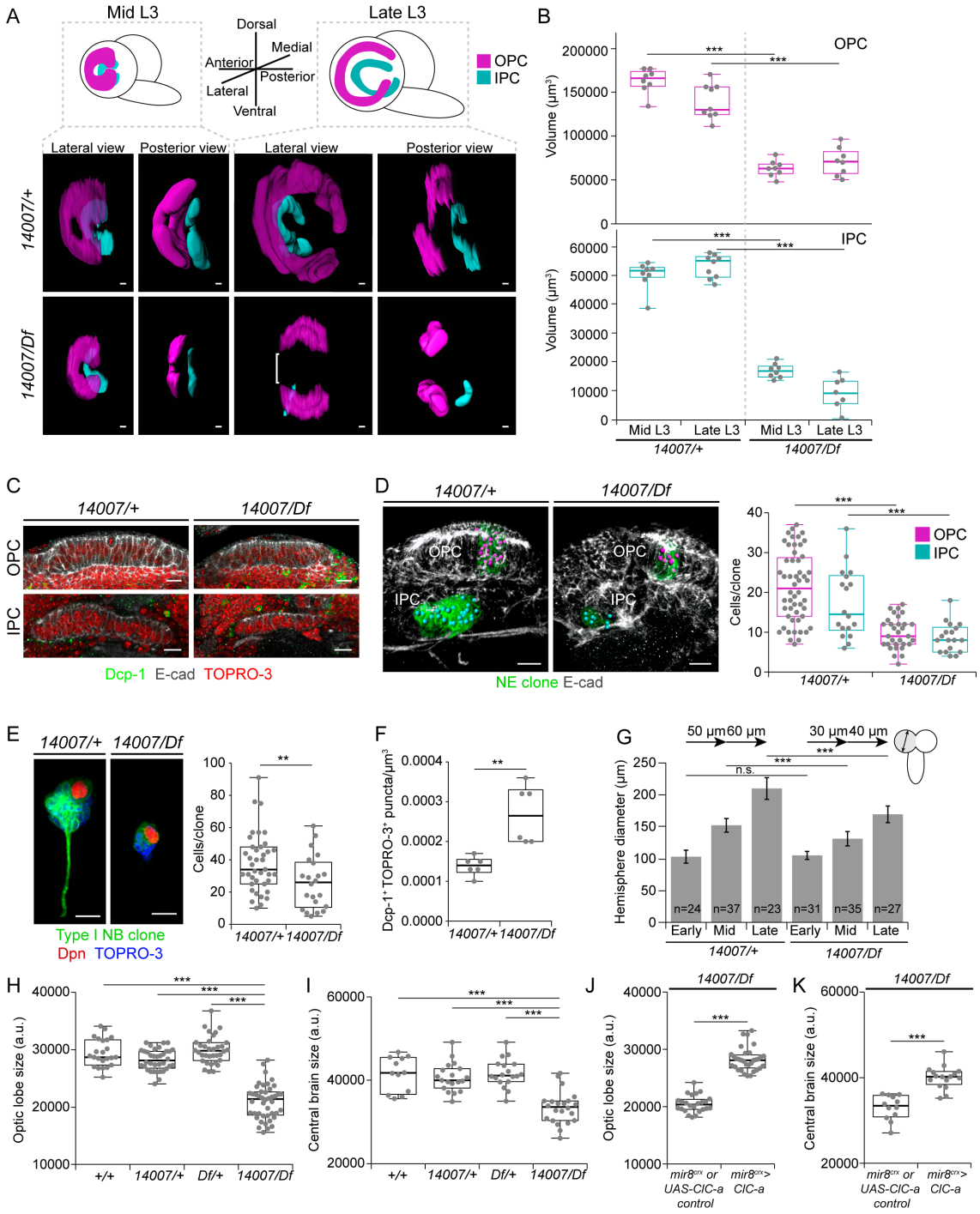

1581

1582

1583

1584

1585

1586

Figure 5

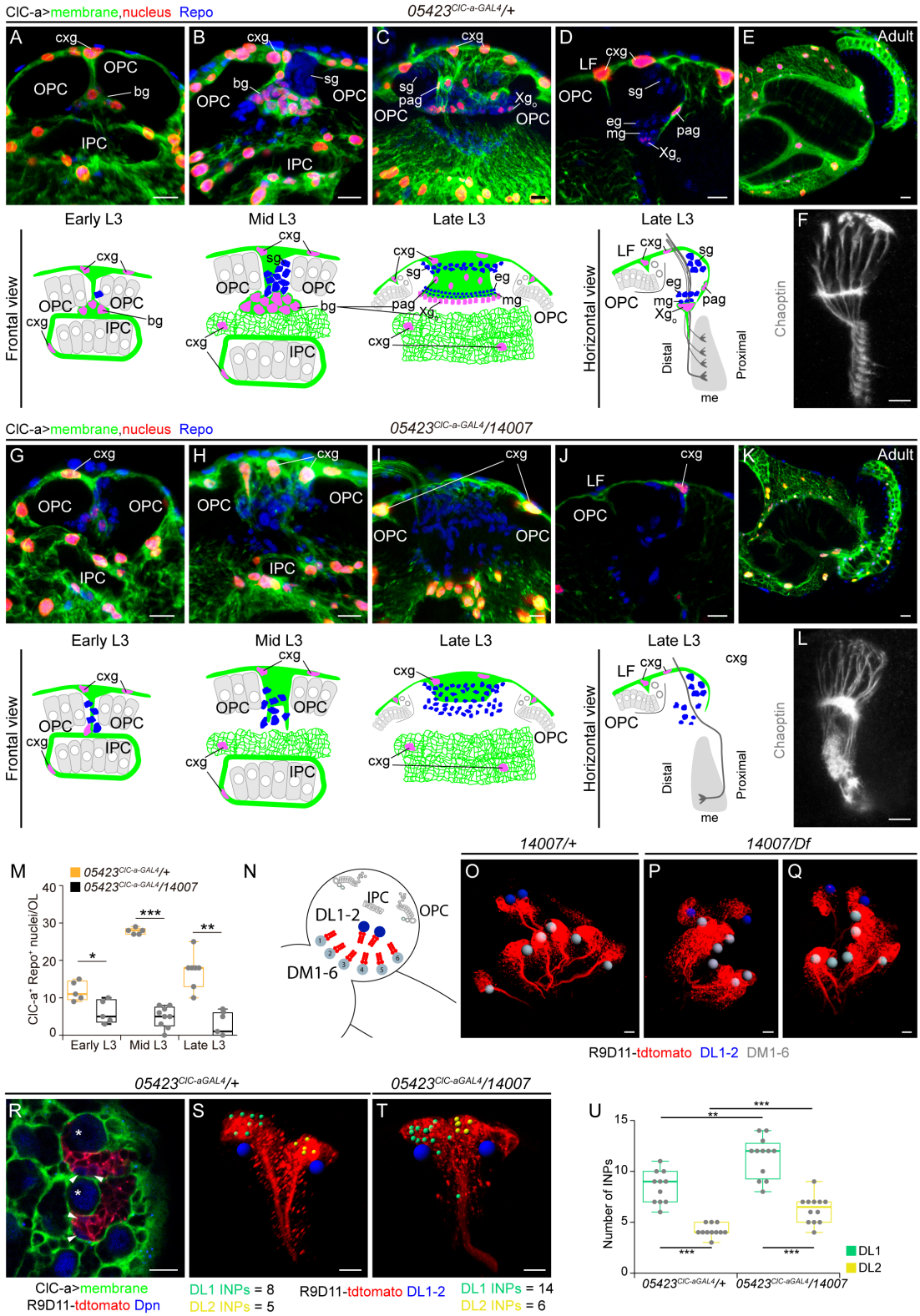
ClC-a>membrane,nucleus Repo
05423ClC-a-GAL4/+
A
B
C
D
E
Adult
cxg
OPC
bg
IPC
sg
pag
Xg
LF
eg
mg
Early L3
Mid L3
Late L3
Frontal view
Horizontal view
Distal
Proximal
me
F
Chaoptin
ClC-a>membrane,nucleus Repo
05423ClC-a-GAL4/14007
G
H
I
J
K
L
M
05423ClC-a-GAL4/+
05423ClC-a-GAL4/14007
ClC-a+ Repo+ nuclei/OL
Early L3
Mid L3
Late L3
N
DL1-2
DM1-6
14007/+
14007/Df
O
P
Q
R9D11-tdtomato DL1-2 DM1-6
05423ClC-aGAL4/+
05423ClC-aGAL4/14007
R
S
T
U
Number of INPs
DL1
DL2
ClC-a>membrane
R9D11-tdtomato Dpn
DL1 INPs = 8
DL2 INPs = 5
R9D11-tdtomato DL1-2
DL1 INPs = 14
DL2 INPs = 6

1591 **Figure 6**

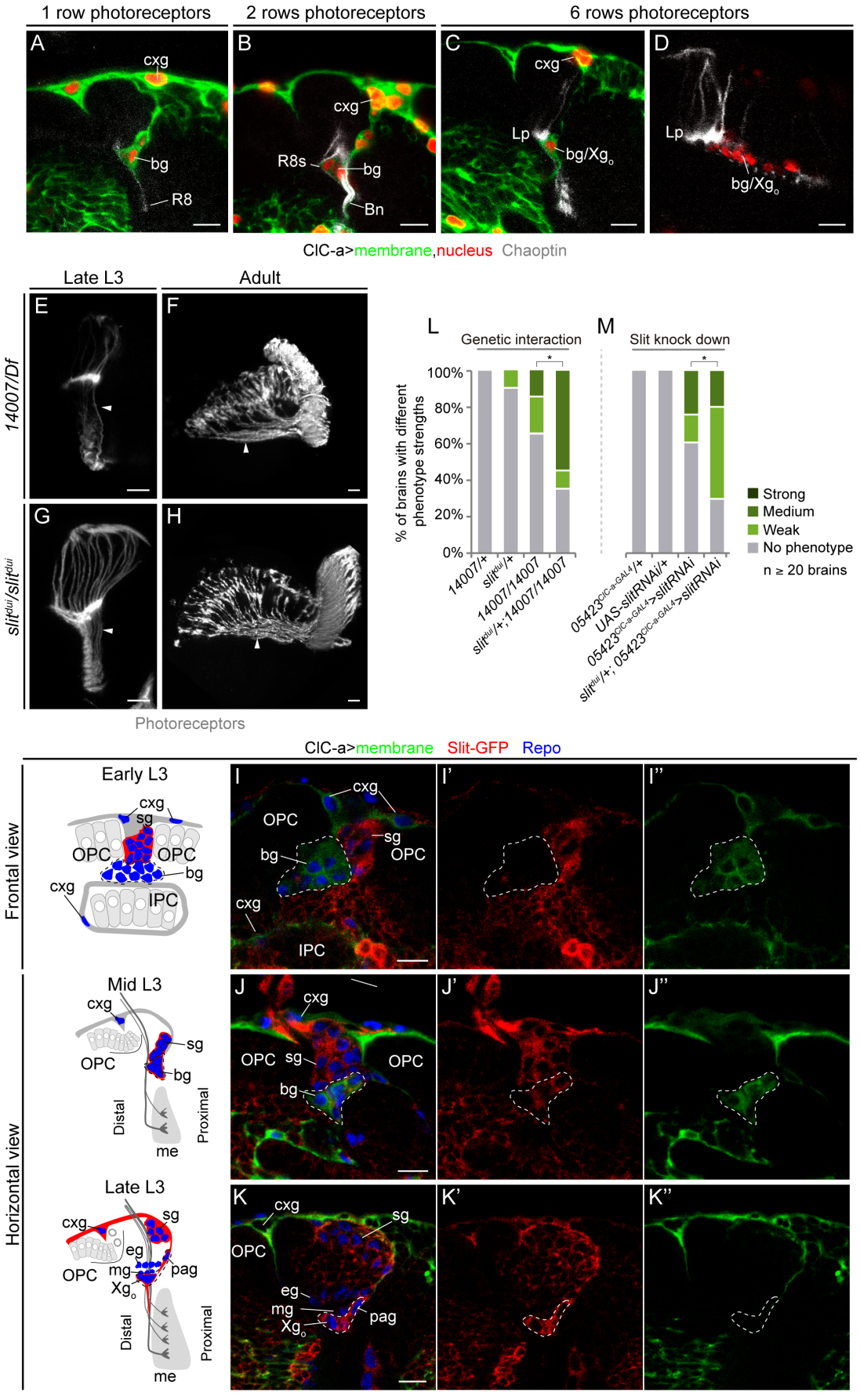

1592

1593 **Figure 7**

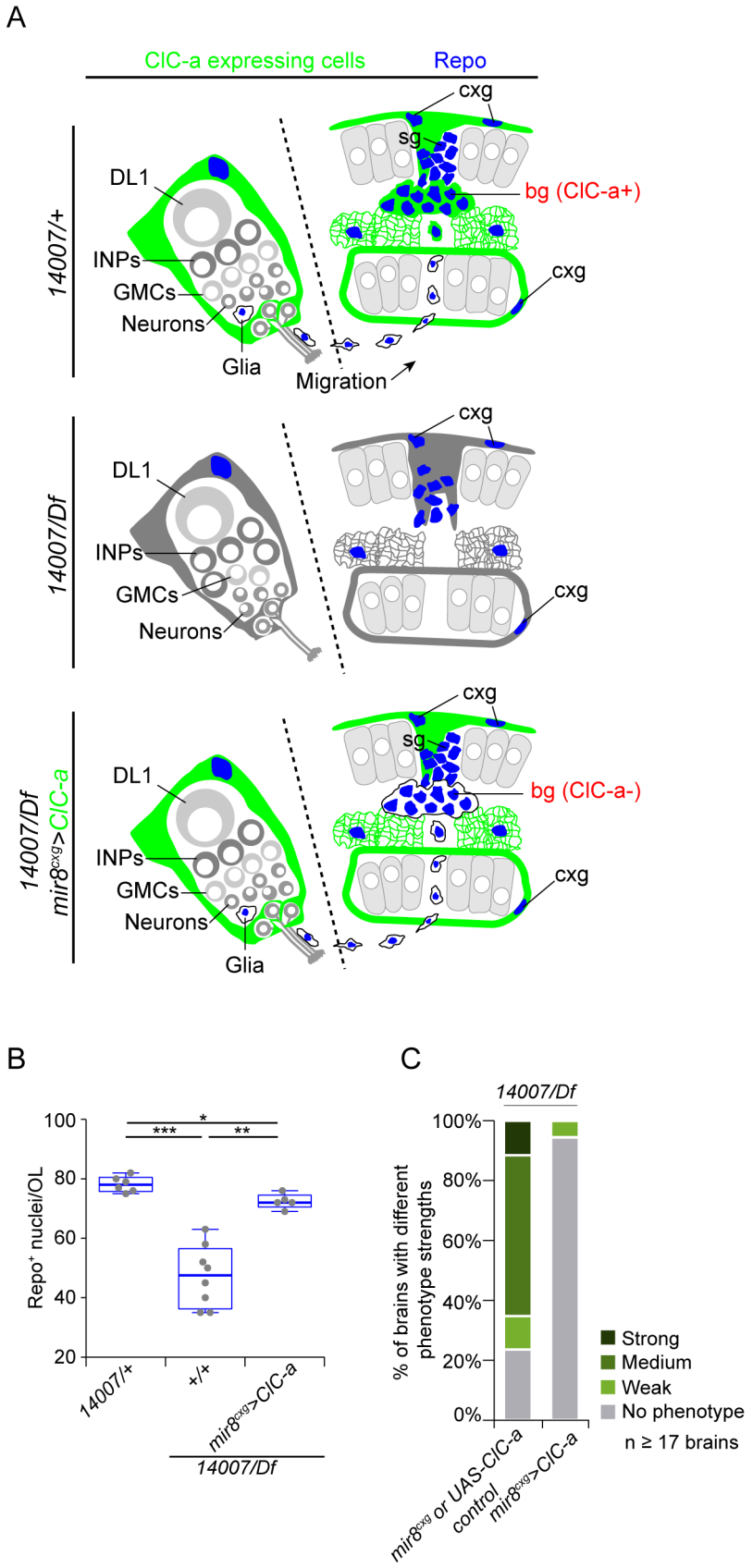

1594

1595

1596 **Figure 8**

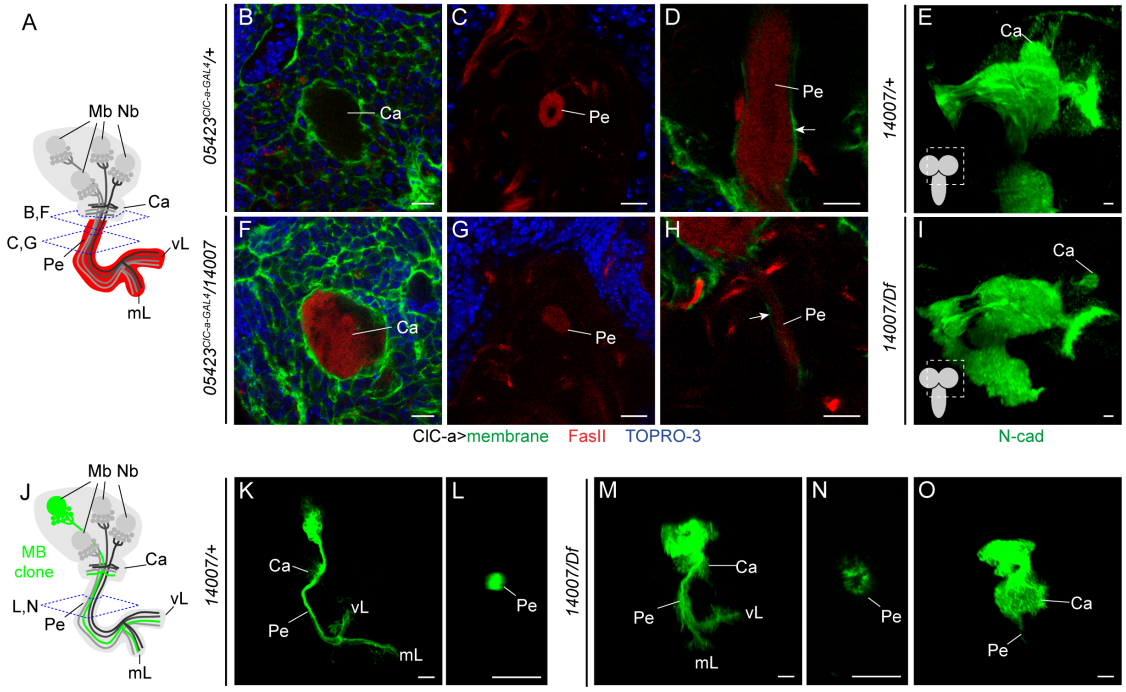

1597